

What Happens to MnO_2 When It Comes in Contact with Zn^{2+} ? An Electrochemical Study in Aid of Zn/ MnO_2 -Based Rechargeable Batteries

Francesca Rossi, Emanuele Marini, Marco Boniardi, Andrea Casaroli, Andrea Li Bassi, Andrea Macrelli, Claudio Mele, and Benedetto Bozzini*

In the science and technology of electrochemical energy storage, different allotropes of MnO_2 , fabricated with a variety of methods, are assembled into electrodes, playing the role of cathode or oxygen reduction reaction (ORR) electrocatalyst. Often, MnO_2 -based cathodes are combined with Zn anodes into different types of batteries, resulting in contact between MnO_2 and its electrochemical reaction products, and Zn^{2+} . Awareness is growing that this interaction adversely affects the functional performance of MnO_2 , but no definitive understanding has been reached for this issue. This study contributes, through electrochemical measurements accompanied by microscopy and Raman spectroscopy, to a better understanding of the way the electrochemical behavior of two technologically representative types of manganese dioxide - hydrothermally grown α - MnO_2 and electrodeposited γ - MnO_2 (EDM) - is degraded when these materials are exposed to neutral and alkaline aqueous solutions, containing Zn^{2+} . Specifically, we highlighted different types of irreversible changes in electrochemical response, which can be interpreted with phase-formation processes. Such changes result in the deactivation of α - MnO_2 as ORR electrocatalyst, and of both α - MnO_2 and EDM as zinc-ion battery (ZIB) cathodes. The electroactivity of EDM for ZIB operation can be restored if Mn^{2+} is added to the neutral electrolyte, because a phase, active in discharge, is electrodeposited during charging.

chemistries, such Na-, Mg-, and Ca-based ones,^[1] exhibit processing and safety issues that are closely cognate to those of Li-based ones. Less aggressive, but potentially competitive Zn-based chemistries with aqueous electrolytes, instead, bear the realistic promise of intrinsic safety, totally green, and easily recyclable components.^[3–5] Rechargeable batteries with Zn anodes can be implemented in three main variants, according to the kind of cathodic process: Zn–air batteries (ZAB),^[6–8] Zn-ion batteries (ZIB),^[9,10] and rechargeable alkaline batteries (RAB).^[11]

The three cathodic chemistries of ZABs, ZIBs, and RABs can be supported by different crystallographic types based on MnO_2 , or its partial reduction products, considering, on the one hand, intercalation of the pristine material and, on the other hand, the involvement of Mn in the electrochemically relevant redox processes. In this sense, ZABs, ZIBs, and RABs can be regarded as different implementations of the Zn/ MnO_2 system.

Batteries based on Zn and MnO_2 are considered as a prospective integration of, or

alternative to, LIBs owing to: i) abundance of Zn and Mn (they are the 24th and 12th most abundant elements in Earth crust, respectively); ii) cost (Zn = 2.9 USD kg⁻¹ and Mn = 2 USD kg⁻¹ vs Li = 17.5–19.8 USD kg⁻¹ and Co = 59.6 USD kg⁻¹),^[12] and iii) sustainability (both Mn and Zn are not considered “critical raw materials”), combined with iv) non-toxicity^[13,14] and v) stability

1. Introduction


In a battery scenario dominated by lithium-ion battery (LIB) technology, awareness of the different types of well-described criticalities and suboptimalities of this class of chemistries is driving the development of post-Li concepts.^[1,2] Among these, several

F. Rossi, C. Mele
Departement of Innovation Engineering
University of Salento
73100 Lecce, Italy

E. Marini
Brennstoffzellen Grundlagen (ECC)
Zentrum für Sonnenenergie- und Wasserstoff-Forschung
Baden-Württemberg (ZSW)
89081 Ulm, Germany

M. Boniardi, A. Casaroli
Department of Mechanics
Politecnico di Milano
20156 Milano, Italy

A. L. Bassi, A. Macrelli, B. Bozzini
Department of Energy
Politecnico di Milano
20156 Milano, Italy
E-mail: benedetto.bozzini@polimi.it

 The ORCID identification number(s) for the author(s) of this article can be found under <https://doi.org/10.1002/ente.202200084>.

© 2022 The Authors. Energy Technology published by Wiley-VCH GmbH. This is an open access article under the terms of the Creative Commons Attribution License, which permits use, distribution and reproduction in any medium, provided the original work is properly cited.

DOI: 10.1002/ente.202200084

in aqueous electrolytes. Moreover, the Zn anode and the MnO₂ cathode exhibit high gravimetric theoretical capacities (820 and 616 mAh g⁻¹, respectively), considering the two-electron process for the latter compound).^[6,15]

In addition, all ZAB, ZIB, and RAB technologies enable the use of aqueous electrolytes of different pHs. ZABs and RABs typically employ strongly alkaline solutions and ZIBs neutral ones: recent research is addressing the use of neutral electrolytes also for ZABs. The pH of the electrolyte has a strong impact on stripping/plating of Zn: neutral conditions stabilize the Zn²⁺ aquo complexes, minimizing precipitation of ZnO from zincate solutions,^[16] which is typical of alkaline chemistries^[17] and impacts anode cyclability.^[18–21]

MnO₂ exhibits a variety of polymorphs, resulting from the arrangement of the MnO₆ fundamental units. Polymorphs are categorized as: tunnel-type (α or cryptomelane, β and todorokite), layered (δ), and spinel (λ) phases.^[15] α -MnO₂ has been widely investigated for ZIB applications,^[15,22–26] but this phase is appealing also for the air gas diffusion electrode (GDE) of ZABs,^[27] especially for oxygen reduction reaction (ORR). This polymorph is constituted by one-dimensional 2 × 2 tunnels (0.46 × 0.46 nm²), that are believed to enable a reversible intercalation of Zn²⁺, with typical capacities of the order of 200 mAh g⁻¹.^[24–26,28,29] Another form of electrochemically active MnO₂, commonly used in alkaline batteries, is electrodeposited γ -MnO₂, often denominated electrodeposited manganese dioxide (EDM). This form of MnO₂ exhibits a structure that can be described as a microscopic intergrowth between the pyrolusite (β -MnO₂) and ramsdellite polymorphs (R-MnO₂).^[30] The structure of EDM is in fact more complex, owing to the presence of cation vacancies, lower valent manganese species, and structural water.^[31,32] Thus, the chemical composition of γ -MnO₂ can be described as: (Mn⁴⁺)_{1-x-y}(\square)_x(Mn³⁺)_y(O²⁻)_{2-4x-y}(OH⁻)_{4x+y}, where \square represents a cation vacancy, while x and y are the mole fractions of cation vacancies and lower valent Mn³⁺ ions, respectively. Typically, for pristine EDM, x and y range in the intervals of 6%–8% and 4%–12%, respectively.^[30] Structural water is present in the form of protons associated with the O²⁻ ions. Clearly, a wide range of materials can be classified as EDM or γ -MnO₂, according to the details of the synthetic route.

In ZABs and RABs, unless ideal ion-specific separators are used, MnO₂ is expected to come in contact with Zn²⁺, in one of the different solvation forms, resulting from pH-dependent speciation. In the case of ZIBs, contact of MnO₂ with Zn²⁺ is instead necessary for the intercalation process to take place. The research community is becoming progressively aware of the fact that the poorly understood interaction of Zn²⁺ with MnO₂ can trigger crucial cathode degradation processes. This issue has been only partially addressed in the literature. In the case of alkaline solutions – such as those used for ZABs and RABs –, hetaerolite ZnMn₂O₄ has been reported to form an irreversible phase at the cathode of alkaline batteries.^[33–36] This side product is the result of the chemical reaction between Zn(OH)₄²⁻ and MnOOH: the anodic and cathodic reaction products, respectively. Hetaerolite ZnMn₂O₄ is highly resistive and notably electrochemically inert, thus impairing the recharge process. In neutral solutions – typically used for ZIBs and of prospective interest for ZABs –, the most commonly reported

mechanism is reversible Zn²⁺ ion intercalation/deintercalation, which involves a reversible phase transition from tunnel-structured α -MnO₂ to layer-structured Zn-birnessite, spinel ZnMn₂O₄, or layered Zn-buserite.^[37] A layer-type MnO₂ (δ -MnO₂), where Zn²⁺ can intercalate into the structure, shows different structural evolution patterns because of the diversity of δ -MnO₂ phases (e.g., chalcophanite, birnessite, buserite, and vernadite): this results in joint incorporation of cations and water molecules within the interlayer. For example, spinel-type ZnMn₂³⁺O₄ was observed when nano-flake δ -MnO₂ was used in an aqueous electrolyte,^[28] while a reversible variation of MnO₂/ZnMnO₂ was observed for hydrated δ -MnO₂ in a non-aqueous solution.^[38] At variance with this approach, Sun et al.^[37] proposed H⁺ and Zn²⁺ cointercalation in akhtenskite-structure MnO₂ (ϵ -MnO₂). The consecutive formation of the MnOOH and ZnMn₂O₄ strongly promotes this mechanism of insertion of H⁺ followed by Zn²⁺. In addition to redox-related intercalation and phase transition, an accompanying precipitation process was recognized, which leads to the formation of inactive Zn₄(OH)₆(SO₄)·5H₂O (ZHS) on the surface of α -MnO₂: this is a loose precipitate, which can be removed by rinsing.^[39,40] On the contrary, a recent study^[41] revisited the effect of ZHS formation, proposing a complex reversible dissolution-deposition mechanism that contributes to capacity.

In this article, we face explicitly the issue of assessing the impact of the presence of Zn²⁺ in electrolytes of practical interest on the functional behaviour of two types of MnO₂. Regarding the type of MnO₂, we considered two different forms: an emerging polymorph and a traditional material. The first type is α -MnO₂, which is regarded as a promising ORR electrocatalyst in alkaline^[27] and neutral ZABs^[42,43] as well as ZIB cathode^[44] in neutral electrolyte. The second type is (EDM) of the γ -MnO₂ type, reported as ZIB cathode.^[15,45] This study is centered on electrochemical measurements, comparing systematically the behavior of MnO₂ in the absence and in the presence of Zn²⁺, complemented by microscopy and Raman spectroscopy.

2. Experimental Section

2.1. Materials

2.1.1. Electrolytes

In this work, a range of aqueous electrolytes, typical of battery operation, electroanalytical testing and electrodeposition of electrode materials are employed. Specifically: i) alkaline electrolytes for tests relevant to ZAB and RAB conditions: 0.1 M KOH without and with 1 mM ZnO: this concentration of KOH ensures high solubility of both O₂ and ZnO; ii) Neutral electrolytes for ZIBs: ii.a) 0.1 M Na₂SO₄; ii.b) 0.1 M ZnSO₄; ii.c) 0.1 M ZnSO₄ + 4 mM MnSO₄; ii.d) 2 M ZnSO₄; ii.e) 2 M ZnSO₄ + 4 mM MnSO₄; ii.f) 0.1 M Na₂SO₄ + 1 mM ZnSO₄; ii.g) 0.1 M NH₄Cl + 8 mM ZnCl₂ (pH was adjusted with NH₄OH); iii) Acidic for MnO₂ electrodeposition: 0.5 and 1 M H₂SO₄. All the solutions were prepared from analytical-grade chemicals (Sigma-Aldrich) and Milli-Q water (resistivity 18.2 M Ω cm).

2.1.2. Preparation of α - MnO_2 -Based Electrodes

Synthesis of α - MnO_2 : α - MnO_2 nanorods were synthesized by a microwave-assisted (450 Monowave by Anton Paar GmbH) hydrothermal method, following the procedure described in ref. [27]: 314 mg of K_2SO_4 (Sigma-Aldrich), 486 mg of $\text{K}_2\text{S}_2\text{O}_8$ (Sigma-Aldrich) and 203 mg of $\text{MnSO}_4 \cdot \text{H}_2\text{O}$ (Sigma-Aldrich) were mixed together with 10 mL of Milli-Q water into a G30 wide-neck vial (Anton Paar GmbH). The mixture was transferred to the microwave reactor and heated at 200 °C for 30 min under stirring at 600 rpm. The product was collected by centrifugation and washed five times with deionized water, checking the pH of the supernatant, to completely remove the residual acid and water-soluble salts. Finally, the synthesis product was dried overnight in a vacuum oven at 80 °C (VT 6025 vacuum oven by Thermo Fisher Scientific Inc.). The phase structure is pure α - MnO_2 (Figure 1A) and the morphology consists of monodisperse nanorods $\approx 1 \mu\text{m}$ long and $\approx 50 \text{ nm}$ in diameter (Figure 1B).

Figure 1A shows a typical cryptomelane-like pattern having a tetragonal crystal structure with an I4m space group. The diffraction peaks which appeared at $2\theta = 28.7^\circ$, 37.56° , 41.98° , 49.74° , 56.34° , and 60.12° can be perfectly indexed with the diffraction peaks of (310), (211), (301), (411), (600), and (521) crystal planes

of cryptomelane-type α - MnO_2 standard data (JCPDS card PDF file no. 44-0141) and lattice parameters of $a = b = 9.78 \text{ \AA}$, $c = 2.86 \text{ \AA}$.

Drop-Cast α - MnO_2 -Based, Glassy-Carbon Supported, Electrodes: Electrodes for electroanalytical tests were prepared by drop-casting an α - MnO_2 -based ink onto glassy carbon (glassy carbon disk inserts, Pine Research Instrumentation) substrates. The ink was prepared by mixing 8.00 mg of α - MnO_2 , 8.00 mg of C65 carbon black, and 4 mL of Nafion solution (see below for details). The obtained mixture was magnetically stirred for 10 min and then sonicated for 1 min at 10 W with a UP200St ultrasonicator by Hielscher Ultrasonics GmbH. The Nafion solution was prepared by mixing 39.85 mL of Milli-Q water, 10.00 mL of ethanol (EtOH, Sigma-Aldrich), and 0.350 mL 5 wt% Nafion 117 solution (Sigma-Aldrich). The ink was kept under magnetic stirring till it is used. 20 μL of ink were dropcast onto glassy carbon electrodes and dried in the air under rotation at 100 rpm, using the rotating disk electrode (RDE) setup described below, turned with the electrode surface facing upwards.

α - MnO_2 -Based, Carbon-Paper Supported, Electrodes: GDEs and porous electrodes were prepared by spray-coating an α - MnO_2 -based ink onto hydrophobized Toray paper (TGP-H-090, Toray) substrates. The ink was formulated by mixing 90 mg of

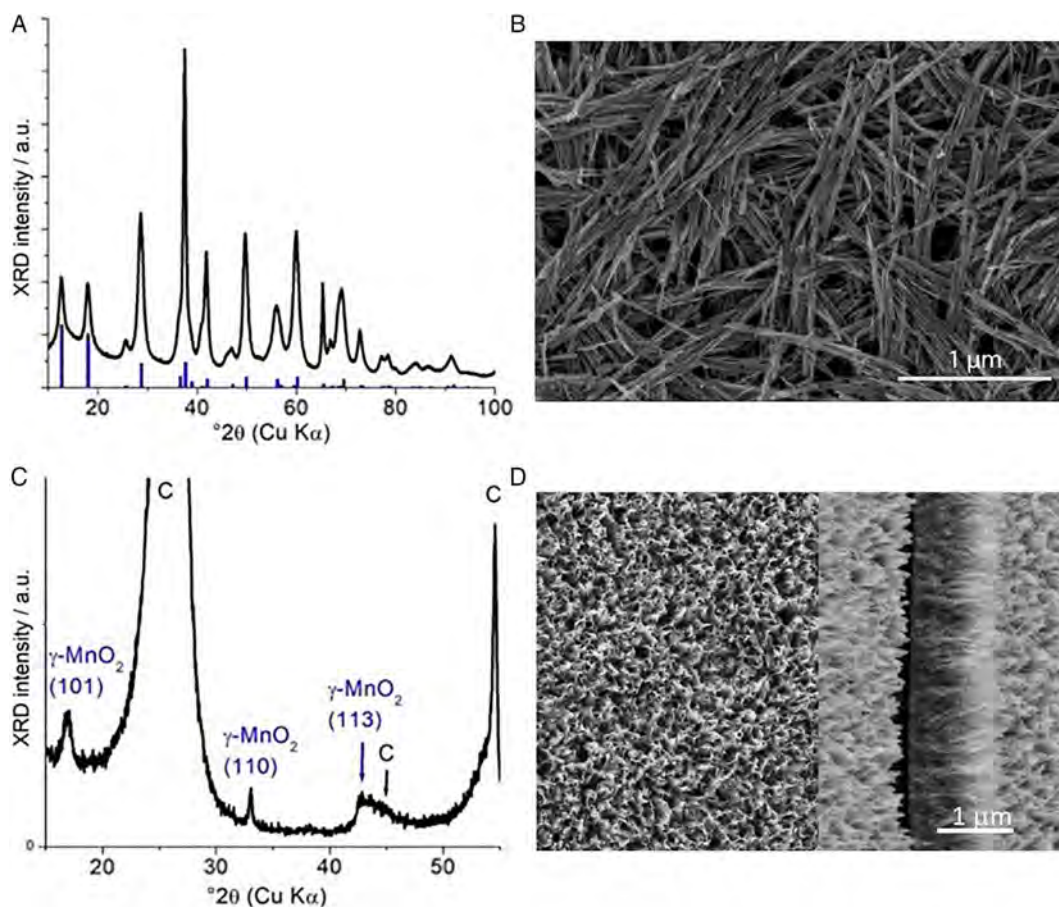


Figure 1. A,C) X-Ray diffractograms and B,D) scanning electron microscope (SEM) micrographs of as-synthesized α - MnO_2 (A,B) and electrodeposited γ - MnO_2 (EDM) (C,D). Blue plots correspond to reflections of reference materials. (B) and (D, left): in-plane and (D, right) cross-sectional images.

α -MnO₂, 90 mg of C65 carbon black, 7.5 mL of EtOH, 7.5 mL of Milli-Q, and 400 mg of the above-mentioned Nafion solution. The mixture was magnetically stirred for 10 min and then sonicated for 2 min and kept under magnetic stirring till usage. The ink was sprayed on the Toray carbon paper support at 80 °C by using a Badger 350 airbrush. The obtained electrodes were dried overnight at 350 °C in a retort furnace (Carbolite Gero Ltd.) under an N₂ atmosphere.

2.1.3. Preparation of Electrodeposited γ -MnO₂ (EDM) Electrodes

EDM was electrodeposited from a 2 M ZnSO₄ + 0.2 M MnSO₄ aqueous solution onto carbon fiber paper (TGP-H-090, Toray) with Zn counter and reference electrodes, according to the approach of,^[37] consisting in applying first galvanostatic conditions at 0.2 mA cm⁻² until the threshold of 1.8 V (vs Zn/Zn²⁺) is attained, and then maintaining 1.8 V for 8 h. Figure 1C shows an X-Ray diffractogram of EDM grown on carbon paper, featuring the strong graphite peaks at 26.4°, 44.4°, and 54.5° (JCPDS No. 41-1487), and the characteristic peaks of well-crystallized γ -MnO₂ (JCPDS No. 0644), in keeping with literature on the structure of EDM.^[46,47] The lower relative intensity of γ -MnO₂ peaks with respect to those of the carbon support are, of course, in line with the relative amounts of material and the diffractometer geometry and allow phase identification with the required accuracy. In Figure 1D, we report in-plane and cross-sectional SEM micrographs, showing a rod-shaped columnar morphology.

2.2. Electrochemical Setups

Electrochemical experiments – centered on cyclic voltammetry (CV) and linear-sweep voltammetry (LSV) – were carried out with VersSTAT 3F and BioLogic VMP-300 potentiostats in different setups, according to the specific purpose, detailed in the Results and Discussion Section. CV was employed for the study of MnO₂-based materials relevant to ZIB fabrication and operation, while LSV was used for ORR electrocatalytical investigations. Regarding the choice of the anodic and cathodic terminal, in the case of CVs, in one type of experiment they encompass the Mn redox range from Mn(IV) to Mn(II), and in a second one, they span the ZIB operating range. In the case of LSVs, instead, they enable to assess accurately the ORR onset and limiting current density – when expressed – minimizing the reaction of the MnO₂ catalyst. The scan rates conform to the literature and are such as to enable a degree of development of the mass-transport processes allowing accurate peak detection.

i) *Three-electrode cell* equipped with an Ag/AgCl (3.5 M KCl) reference electrode, Pt or carbon-rod counter electrodes, and Pt or glassy carbon working electrodes. The glassy carbon electrode was regenerated by mechanical polishing and the Pt electrode by treatment with concentrated HNO₃ prior to each experiment: the surface conditions were checked by CV in the pure supporting electrolyte.

(ii) *RDE/ Rotating Ring-Disk electrode (RRDE) experiments* were carried out with a device from Pine Research Instrumentation, based on an MSR Rotator. The working electrode supports were Pt or glassy carbon disks (0.2 cm²), the ring electrode was Pt, and

the cleaning consisted in polishing with 0.3 μ m alumina on microcloth. When electrolytes containing Zn²⁺ were employed, complete re-polishing with 600 grit silicon carbide paper was needed to restore the pristine condition of the electrode support, which was checked by CV in 0.1 M Na₂SO₄ supporting electrolyte. The glassy carbon (GC) cleaning procedure and explicit verification of surface conditions by CV were found to be crucial for the consistency and reproducibility of both electrodeposition and electrocatalysis experiments. The reference electrodes were Ag/AgCl (3.5 M KCl) and Hg/HgO (4.3 M KOH), for neutral and alkaline electrolytes, respectively. The counter electrode was a Pt spiral.

iii) *ORR electrocatalysis experiments* were carried out with the following protocol: electrolyte aliquots of 150 mL, hosted in a dedicated cell for RRDE/RDE, closed to exchange with ambient air, were outgassed with Ar bubbling for at least 20 min and 10 CV cycles were measured in the range 0.3 \div -0.5 V_{SHE} at 5 mV s⁻¹ at 1600 rpm. Then, the solution was saturated with O₂ for at least 20 min and the same CV measurements were performed. Immediately afterward, LSV measurements were performed on the disk in the same potential range as the CVs, setting the ring potential at 0 V_{SHE}, for RRDE experiments. The rotation rate was increased in steps from 100 to 1600 rpm. ORR measurements were repeated thrice, for statistical robustness.

2.3. Morphological and Structural Characterization

The phase structure of MnO₂ samples was characterized by powder X-Ray diffraction (XRD) taken with a RIGAKU, SMARTLAB SE system operating at 3 kW with Cu α radiation and a Ni filter to suppress the $k\beta$ line. The SmartStudio II software from Rigaku was used to extract the parameters of interest from measured θ –2 θ scans.

The vibrational structure of MnO₂ samples was investigated by Raman Spectroscopy using two systems, that yielded perfectly coherent results. The first one was a Jobin Yvon Horiba LabRam confocal system using the excitation at 633 nm provided by a He–Ne laser delivering 7 mW at the sample surface, and equipped with a 10 \times objective. The Raman spectra were acquired with a 600 grid mm⁻¹ spectrometer. The second spectrometer was a Renishaw inVia Raman microscope with a diode-pumped solid-state laser (λ = 660 nm), 1800 L mm⁻¹ grating, and 50 \times objective.

SEM observations were made on a Zeiss Supra 40 under a high vacuum. The microscope is also equipped with a microanalysis apparatus for energy dispersive spectroscopy (EDS) elemental analysis (Oxford Instruments).

3. Results and Discussion

3.1. A Schematic Framework for the Description of MnO₂ Electrochemistry in Aqueous Solutions

As witnessed by the immense relevant literature, including a number of reviews that have been published over the decades, as well as very recently,^[48,49] the electrochemistry of MnO₂ in aqueous ambient is quite complex and varied. In fact, it strongly

depends on: specific crystallographic type, pH, and electrolyte composition. This rich scenario eases a plethora of aimed discussions of very specific issues and systems, which seldom contribute to a general understanding of the redox reactions of this class of materials.

Notwithstanding a notable scatter of information, important commonalities and regularities of electrochemical patterns can be recognized. If appropriately organized and expounded, these are liable to provide a useful reference framework for research and reporting of experimental results. Specifically, the sequence of voltammetric features found with different MnO₂-based systems might be a helpful benchmark. Out of a huge number of publications – that yield cognate information –, we selected, as a reference case, the prototypical case of the CV of birnessite electrodeposition onto SnO₂ from a neutral, deaerated Na₂SO₄ 0.4 M, MnSO₄ 4 mM, as reported in ref. [50] (Figure 2A). In fact, this measurement exhibits the sequence of redox processes that can be regarded as comprehensive, in that it exhibits all expected valence changes and mixed-valence compounds that can be expected from equilibrium considerations (Figure 2B).

We shall, thus, use it as a terminological basis to reference for our discussion of experimental voltammetric features, the sequence of peaks, and valence transformations schematized in Figure 2A. More details on the literature concerning the assignment of voltammetric peaks to specific redox processes can be found in Section S1, Supporting Information.

3.2. Impact of Zn²⁺ on the Electrochemical Behavior of α-MnO₂ in Neutral Aqueous Solution: Case of ZIB Degradation

In this section, we report on the electrochemical performance of α-MnO₂-based electrodes, fabricated as detailed in Section 2.1.2. In Figure 3, we report CVs measured at drop-cast α-MnO₂ electrodes, in contact with three neutral solutions containing species that, in principle, can be intercalated (Na⁺ and Zn²⁺, as well as, potentially, of protons, notwithstanding the neutral pH) – but can

also lead to the formation of new, Zn(II)-containing phases – into α-MnO₂ and anodically electrodeposited (Mn²⁺).

The experiments have been triplicated and prove perfectly reproducible (only one curve is shown, for clarity). The selected voltage range for voltammetric cycling encompasses the Mn(II)-Mn(IV) redox.

In 0.1 M Na₂SO₄ (Figure 3A), the cathodic behavior is controlled by the C3-type process, generating Mn(II)_{aq/solid}, while the initial anodic behavior comprises the classical sequence of processes leading from Mn(II)_{aq/solid} all the way to MnO₂. No voltammetric feature could be detected, that can be assigned to intercalation processes. Drastic decrease of the current density (c.d.) after the first cycle, and continuing with cycling, denotes progressive redox deactivation of cryptomelane, probably due to some kind of structural rearrangements that warrant more insightful investigation.

If Zn²⁺ is present in the solution (Figure 3B), a small C1-type feature is seen, followed by a sharp C2-type peak, dominating the cathodic branch in the first cycle. This peak disappears upon further cycling. This behavior denotes an irreversible solid phase transformation. The anodic processes are suppressed after the first cathodic-going scan.

If both ZnSO₄ and MnSO₄ are present in the solution (Figure 3C), again a C2-type peak is found to dominate the first cathodic scan, followed, going more cathodic, by a sequence of cathodic peaks. Cycling of α-MnO₂ in the investigated potential range in the neutral electrolyte, even in the presence of added Mn²⁺, evidently leads to the formation of redox-inactive phases. In the absence of Zn²⁺, the inactive species probably contain large proportions of Mn(II), while in its presence Mn(III) is stabilized. It is worth noting that redox deactivation of α-MnO₂ upon cycling in a voltage range encompassing cathodic and anodic processes, is found also in alkaline ambient (see Section S2, Supporting Information).

The results of Figure 3, obtained by cycling in an extended potential range, were compared to those obtained by cycling in the voltage range that is typical of ZIB operation.^[51] This

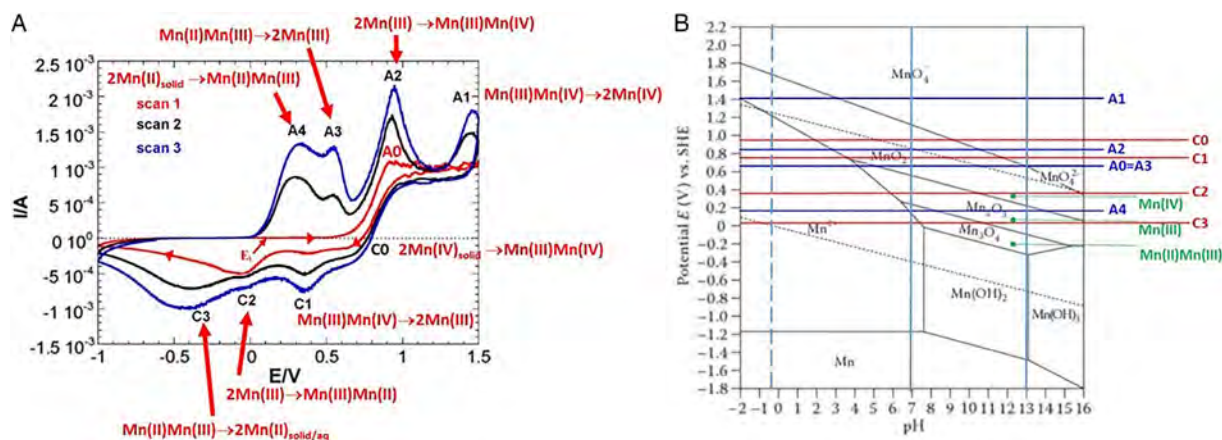


Figure 2. A) Cyclic voltammetry (CV) for birnessite electrodeposition onto SnO₂ from a neutral, deaerated Na₂SO₄ 0.4 M, MnSO₄ 4 mM solution, with a scan rate of 10 mV s⁻¹. Potentials are reported in the Ag/AgCl scale. Subsequent scans are color-coded as indicated in the image. Adapted with permission.^[50] Copyright 2008, Elsevier. B) Pourbaix diagram of the Mn/H₂O system at room temperature, with the indication of the potentials corresponding to the voltammetric features of Panel (A) and of the pH conditions considered (full lines: both main text and Supporting Information; dashed line: only Supporting Information).

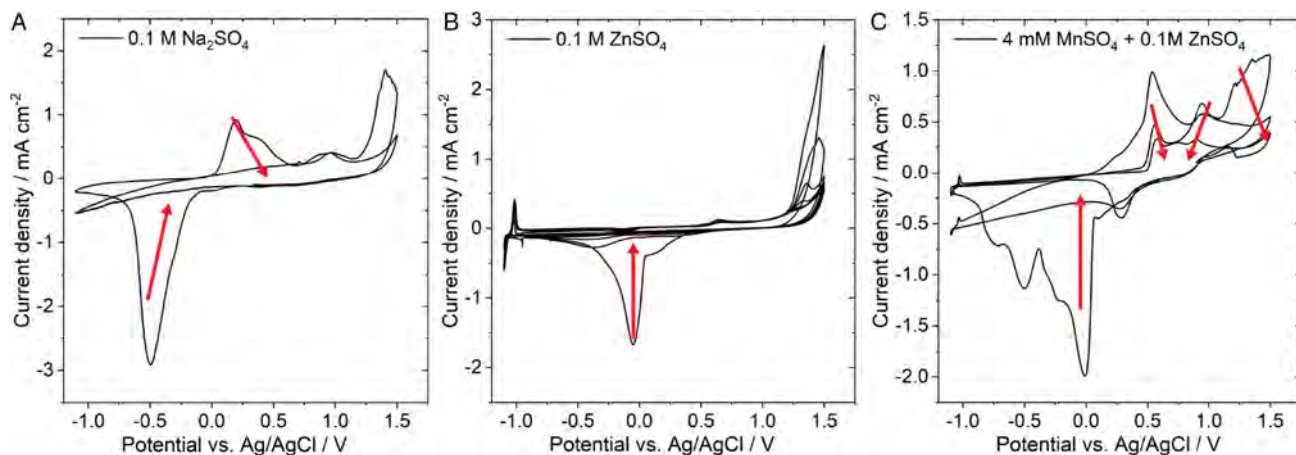


Figure 3. CVs of drop-cast α -MnO₂ electrodes in different neutral electrolytes: A) 0.1 M Na₂SO₄; B) 0.1 M ZnSO₄; C) 0.1 M ZnSO₄ + 4 mM MnSO₄. Scan rate 10 mV s⁻¹.

comparison was carried out in neutral electrolytes containing: Na₂SO₄ (potentially intercalating Na⁺), MnSO₄ (potentially supporting oxidative electrodeposition from aqueous Mn²⁺), and ZnSO₄ (potentially either intercalating Zn²⁺ or forming a new phase upon reaction with α -MnO₂). For clarity of presentation, **Figure 4** reports the CVs (one out of at least three very reproducible replicates) recorded in the ZIB potential range overlapped with the CVs of Figure 3. It can be noticed that, coherently with the peak positions found in Figure 3, the ZIB operating range corresponds to one of limited redox activity. In Na₂SO₄ and MnSO₄ + ZnSO₄ solutions, pseudocapacitive behavior is observed, while in the electrolyte containing only ZnSO₄ the same irreversible peak of Figure 3B can be observed, vanishing after the first cycle. Since the practically relevant potential range contains only the onset of a cathodic reaction, in this particular system, we confirmed this behavior by extending slightly the cathodic range (see the red curve of Panel (C)) beyond that typical of ZIB operation.

To assess changes in morphology and structure of α -MnO₂, pristine electrodes were subjected to prolonged polarization in

the Na₂SO₄ and ZnSO₄ electrolytes at potentials representative of aging under ZIB operating conditions: 8 h at 0.1 V_{Ag/AgCl}, corresponding to discharge, followed by 8 h at 0.9 V_{Ag/AgCl}, corresponding to a discharge–charge cycle. The samples aged under these conditions were subjected to SEM/EDS (**Figure 5**) and Raman (**Figure 6**) analyses. The morphology of the pristine α -MnO₂ electrode (**Figure 5A**) shows the typical cryptomelane nanorods (highlighted with a white circle, see also **Figure 1B**), together with acetylene black particles. EDS point spectra confirm the presence of: i) Mn, O, and K from cryptomelane; ii) C from the C-black, from the carbon paper support, and iii) F and S, in addition to C and O, from the binder.

After polarization at 0.1 V_{Ag/AgCl} (**Figure 5B**) and at 0.1 and 0.9 V_{Ag/AgCl} (**Figure 5C**) in 0.1 M Na₂SO₄ solution, no appreciable changes in morphology can be noticed. As far as composition is concerned, after aging at 0.1 V_{Ag/AgCl} the weight percent of Mn decreases from \approx 32% to \approx 15%, which can be attributed to the loss of Mn by dissolution under the form of Mn(II)_{aq}. Instead, after the treatment sequence at 0.1 and 0.9 V_{Ag/AgCl}, some Mn is regained, probably by the oxidation of Mn(II)_{aq} back to solid

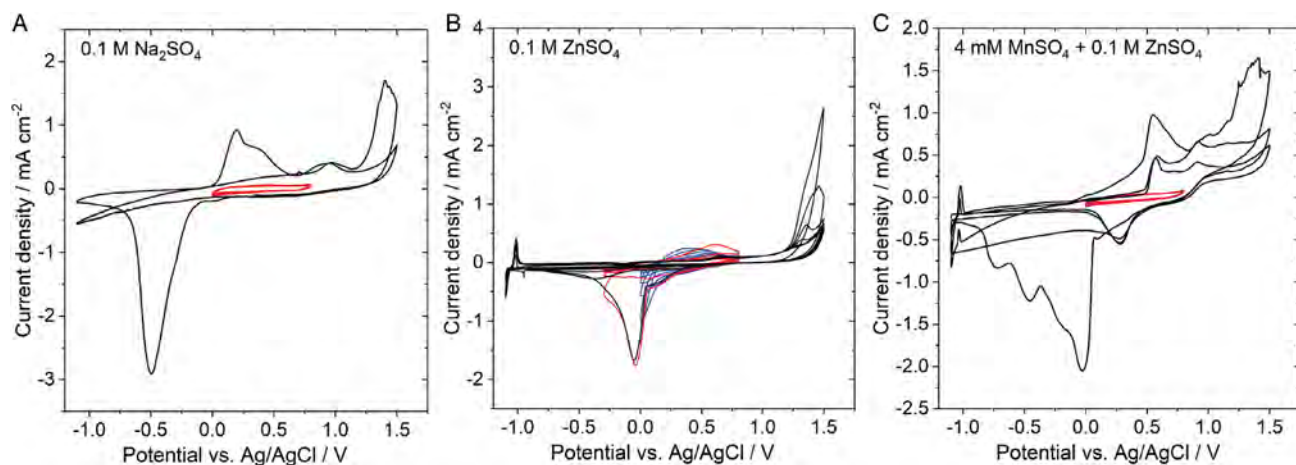


Figure 4. CVs of drop-cast α -MnO₂ electrodes in different neutral electrolytes: A) 0.1 M Na₂SO₄; B) 0.1 M ZnSO₄; C) 0.1 M ZnSO₄ + 4 mM MnSO₄, compared with the CVs of Figure 3. Scan rate 10 mV s⁻¹.

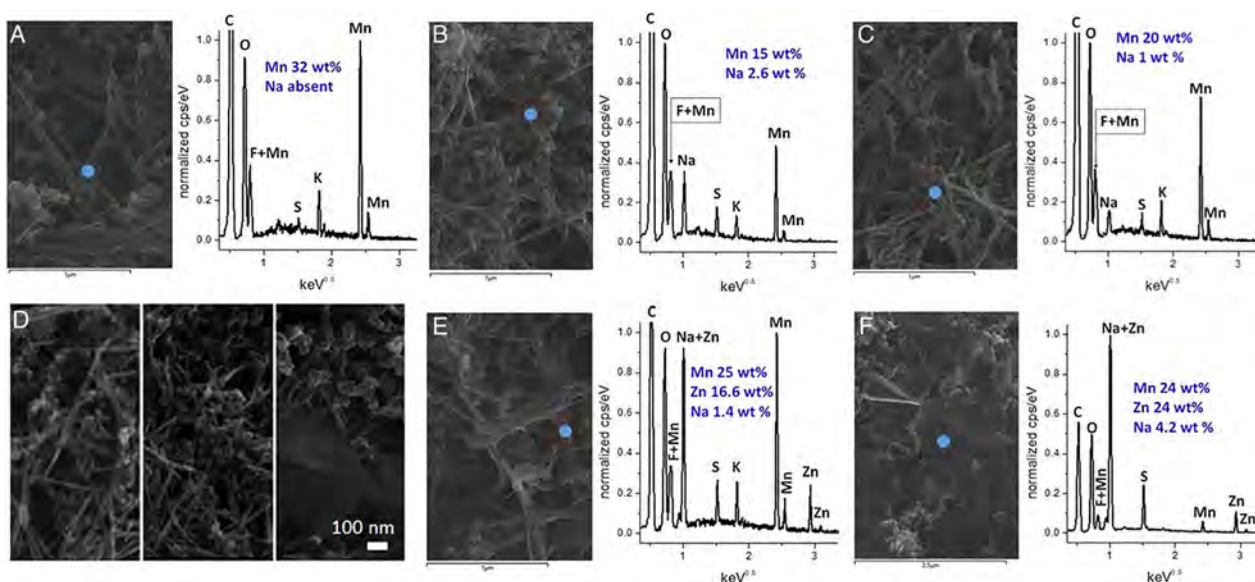


Figure 5. SEM images and EDS spectra of pristine and electrochemically aged α -MnO₂ electrodes. A) Pristine condition. B) After polarization at 0.1 V_{Ag/AgCl} in 0.1 M Na₂SO₄ solution. C) After polarization at 0.1 and 0.9 V_{Ag/AgCl} in 0.1 M Na₂SO₄ solution. D) Details of SEM micrographs of electrodes in pristine conditions and after ageing at 0.1 and 0.9 V_{Ag/AgCl} in 0.1 M Na₂SO₄ and 0.1 M ZnSO₄ solutions. E) After polarization at 0.1 V_{Ag/AgCl} in 0.1 M ZnSO₄ solution. F) After polarization at 0.1 and 0.9 V_{Ag/AgCl} in 0.1 M ZnSO₄ solution.

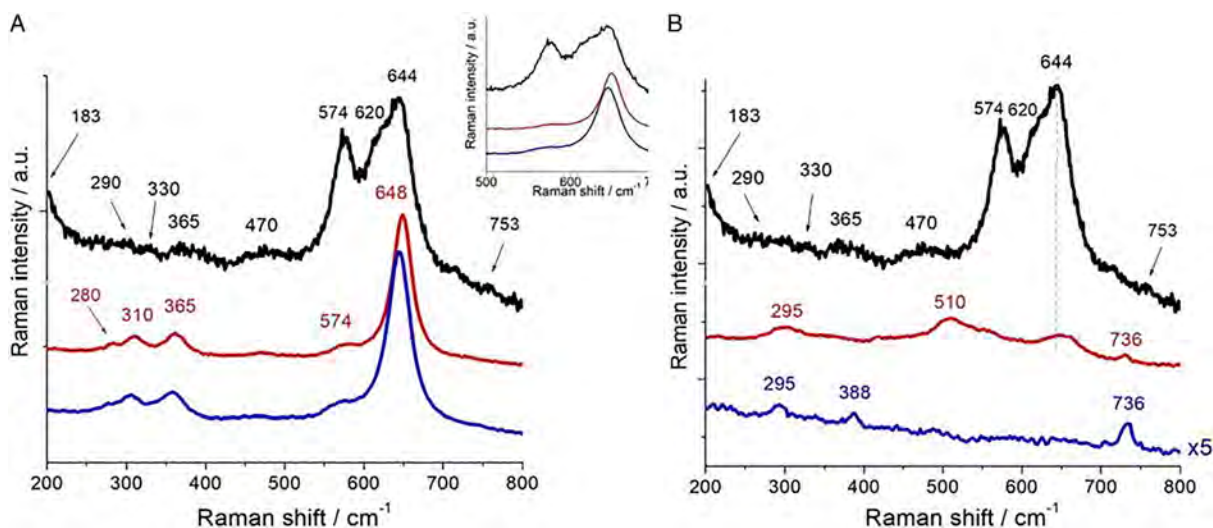


Figure 6. Raman spectra of α -MnO₂ electrodes, pristine (black plots) and electrochemically aged at: (red) 0.1 V_{Ag/AgCl} and (blue) 0.1 and 0.9 V_{Ag/AgCl} in the following solutions: A) 0.1 M Na₂SO₄ and B) 0.1 M ZnSO₄.

MnO₂. Moreover, no Na is found in the pristine sample, but this is instead present in the samples treated electrochemically in the Na₂SO₄ solution. Furthermore, higher relative amounts of Na were found in the samples polarized at 0.1 V than in those polarized subsequently at 0.1 and 0.9 V_{Ag/AgCl}: this scenario is compatible with Na intercalation/deintercalation processes.

After both electrochemical treatments in the Zn²⁺-containing solution, platelet-type structures form (Figure 5E,F). The EDS spectra of these crystallites show the presence of Zn and S: this finding is compatible with the formation of a new phase, such as Zn₄SO₄(OH)₆·4H₂O, recently reported in the literature.^[52] This

result is coherent with the CVs of Figure 4B, as well as the Raman results presented below in this section. The increase of Zn and S content, detected by EDS, confirms that the formation of a new phase is the dominating process, with respect to Zn de-intercalation. Both when only the reduction potential is applied (Figure 5E) and when the reduction and oxidation potentials are applied consecutively (Figure 5F), a progressive increase in the amount of Zn and S is detected. This shows that the new phase tends to form in a wide range of electrochemical conditions, possibly independently from the accompanying Mn redox. Moreover, after polarization at 0.1 V_{Ag/AgCl} in Zn²⁺-containing

solution, the fraction of Mn is lowered, coherently with our findings with Na₂SO₄ solutions, indicating that the presence of Zn²⁺ does not alter appreciably Mn-dissolution. Unlike in the Na⁺ solution, lower amounts of Mn are found after polarizing first at 0.1 V and then at 0.9 V in the Zn²⁺ solution, indicating the anodic deposition of Mn(III)/Mn(IV) species can be affected. This finding correlates with the rapid capacity decay found in Zn²⁺-containing solutions (Figure 4B).

Raman spectra recorded for the same samples are shown in Figure 6. Even though the literature consensus on structure assignment is not universal^[53–58] – probably owing to subtle differences in material synthesis protocols –, the Raman spectrum of pristine α -MnO₂ (black plots) can be regarded to exhibit the following characteristic bands: four strong ones at Raman shifts of ≈ 183 , 574, 620, and 644 cm⁻¹, along with five weak ones at ≈ 290 , 330, 365, 470 and 753 cm⁻¹; these bands are attributed to different kinds of Mn–O lattice vibrations within the MnO₆ octahedral framework. More specifically, the bands at ≈ 330 and 365 cm⁻¹ are attributed to Mn–O bending vibrations in non-corner sharing and corner-sharing positions, respectively. The band at ≈ 574 cm⁻¹ has been assigned to the displacement of the oxygen atoms relative to the manganese ones along the octahedral chains. Changes in intensity of the band at ≈ 644 cm⁻¹ upon ion exchange have been considered to indicate that this band corresponds to Mn–O vibrations perpendicular to the direction of the MnO₆ octahedral double chains.^[54] The presence of both bands at ≈ 574 and 644 cm⁻¹ is thus indicative of a tetragonal structure with an interstitial space consisting of (2 × 2) tunnels. Finally, the band at 753 cm⁻¹ is attributed to antisymmetric Mn–O stretching vibrations.

After polarization at 0.1 V_{Ag/AgCl} in Na₂SO₄ solution (Figure 6A, red curve), a notable change occurs in the spectral pattern. This indicates that prolonged reduction in the ZIB operating range is accompanied by an appreciable structural change, involving all bands of the pristine material. The most evident effect is the important change of relative intensities of the two bands originally located at ≈ 574 and 644 cm⁻¹, accompanied by a blue shift of the latter to ≈ 648 cm⁻¹, together with the disappearance of the band at ≈ 620 cm⁻¹. A definitive assignment of this structural change is not possible on the basis of electrochemical and Raman data alone, but it points in the direction of ion exchange – possibly Na⁺ vs K⁺ – with concomitant disruption of the (2 × 2) tunnel structure.

After subsequent polarization at 0.1 and 0.9 V_{Ag/AgCl} (Figure 6A, blue curve) the highest intensity peak, that blue-shifted as a result of cathodic polarization, undergoes a slight red shift (see inset). This denotes that anodic polarization might have induced a partial structural change toward the γ -MnO₂ form.^[59]

After polarization at 0.1 V_{Ag/AgCl} in the ZnSO₄ solution (Figure 6B, red curve), the prominent group of bands at ≈ 574 , 620, and 644 cm⁻¹ undergoes a notable intensity reduction, accompanied by: i) the disappearance of the bands at lower Raman shifts ≈ 365 cm⁻¹; ii) the appearance of new bands at ≈ 295 , 510 and 736 cm⁻¹, and iii) a slight blue shift of the band originally located at ≈ 644 cm⁻¹.

Furthermore, polarization at 0.1 and 0.9 V_{Ag/AgCl} in the ZnSO₄ electrolyte (Figure 6B, blue curve) brings about further changes in spectral pattern: the bands at ≈ 295 and 736 cm⁻¹ are

strengthened, and those at ≈ 510 and 644 cm⁻¹ disappear and a new one at ≈ 388 cm⁻¹ forms.

Definitive assignment of these changes in the spectral pattern on the basis of literature information is not straightforward and the clarification of mechanistic details is beyond the scope of the present study. This investigation will be undertaken through in situ extended X-ray absorption fine structure (EXAFS), with the approach described in ref. [60] Nevertheless, the observed modification proves that cathodic and cathodic/anodic polarization in Zn²⁺-containing electrolytes brings about evident and progressive structural modifications. Moreover, the observed changes in vibrational structure clearly correlate with the modification of the voltammetric response pinpointed in Figure 4 and the microscopic morphological changes highlighted in Figure 5.

3.3. Impact of Zn²⁺ on the Electrochemical Behavior of EDM in Neutral Aqueous Solution: Case of ZIB Degradation

This section is devoted to the investigation of the effects of Zn²⁺ addition on both the electrodeposition behavior of EDM (Section 3.3.1) and its electrochemical performance. The focus is mainly on the neutral electrolytes of interest for ZIBs, in which Zn²⁺ is necessarily present, but, for the sake of completeness, in the Supporting Information (Section S3, Supporting Information), we also address the impact of Zn²⁺ on the growth of EDM from the traditional strongly acidic solutions.

3.3.1. Cyclic Voltammetric Electrodeposition

In the first set of experiments, we carried out electrodeposition onto glassy carbon electrodes in the potential window 1.5 ÷ -1.0 V_{Ag/AgCl} (see, e.g.^[50,61]), starting from OCP, at a scan rate of 10 mV s⁻¹. For the reasons provided in Section 3.2, we selected electrolytes containing MnSO₄, Na₂SO₄, and ZnSO₄. Measurements were replicated thrice for each condition. Specifically, in **Figure 7**, we report CV measurements: 4 mM MnSO₄ + 0.1 M Na₂SO₄ (Figure 7A); 4 mM MnSO₄ (Figure 7B) and 4 mM MnSO₄ + 0.1 M ZnSO₄ (Figure 7C). Information regarding the impact of Zn²⁺ on the initial stages of EDM growth is reported in the Supporting Information (Section S4, Supporting Information). The structure of samples electrodeposited onto carbon paper from these electrolytes with 20 CV cycles was characterized by Raman spectroscopy (**Figure 8**).

In the electrodeposition experiment from the 4 mM MnSO₄ + 0.1 M Na₂SO₄ electrolyte, reported in Figure 7A), the voltammetric pattern described in Section 3.1 can be found. The main peculiarities here are that, in keeping with,^[61] the peak corresponding to process C0 extends into the potential region of process C1 and the cathodic peaks are sharper and better defined than those of.^[50] Moreover, prolonged cycling disclosed an evolution of the MnO₂-based film that escaped the analyses of,^[50,61] disclosing that the asymptotic CV pattern is the one in which peaks C3 and A4 tend to vanish progressively, while peaks A3 and A2 increase and shift to slightly higher anodic potentials. In correspondence, the c.d. in the cathodic range more negative than C3, is vanishing. The long-term evolution of the CVs seems

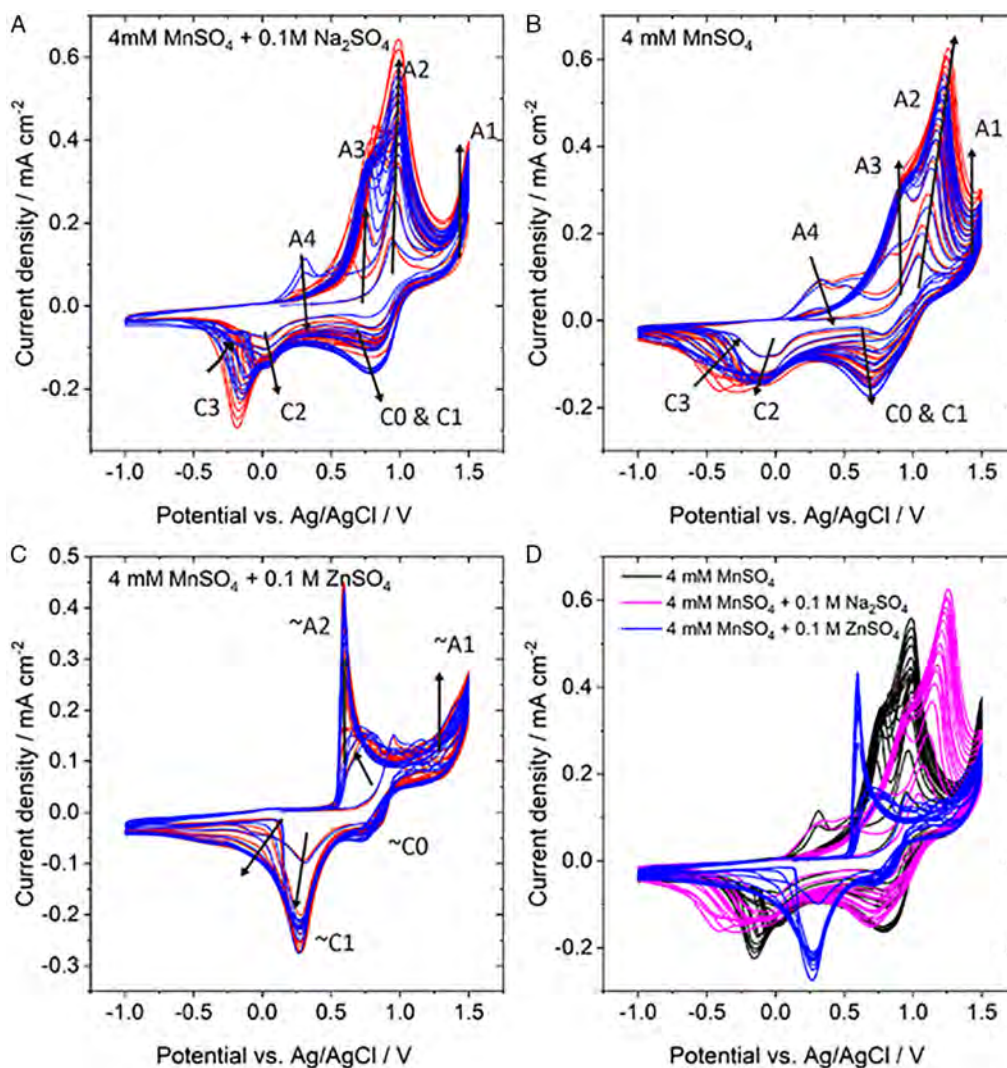


Figure 7. CVs (10 mV s^{-1}) measured at a glassy carbon electrode, in contact with the neutral aqueous electrolytes described below. A) $4 \text{ mM MnSO}_4 + 0.1 \text{ M Na}_2\text{SO}_4$; B) 4 mM MnSO_4 ; C) $4 \text{ mM MnSO}_4 + 0.1 \text{ M ZnSO}_4$. In Panel D), we report the data of Panels (A–C), overlapped, for comparison. Red and blue plots in (A–C) show two out of three independent replicated measurements.

to point toward stabilization of the mixed Mn(II)Mn(III) species, with a lower propensity to the reduction of Mn(II) in the investigated potential range.

The extension of peak C1 into the potential region of peak C1 is compatible with the Na^+ -intercalation reaction, possibly favored by structural differences in the film triggered by the differences in nucleation between GC and SnO_2 . Moreover, the increasing intensity of peak C0–C1 with cycling, correlates with the progressive change in the A3 + A4 pattern, due to structural changes – such as the buildup of inactive Mn_3O_4 – that hinder intercalation. Furthermore, oxide buildup is witnessed by the fact that the anodically consumed charge after prolonged cycling is notably larger than the cathodic one (Figure S2A, Supporting Information). In the Raman spectrum of samples electrodeposited from the $4 \text{ mM MnSO}_4 + 0.1 \text{ M Na}_2\text{SO}_4$ solution (Figure 8, black plot), the bands at ≈ 350 and $\approx 640 \text{ cm}^{-1}$ are compatible with the $\gamma\text{-MnO}_2$ structure.^[59]

Repeating the same experiment in a Na^+ -free electrolyte (Figure 7B) gives rise to marked quantitative changes in a similar qualitative voltammetric pattern. i) Overlapping features C0–C1 and peaks C2, C3 are shifted cathodically. ii) The c.d. in the high cathodic range is appreciably larger in the absence of Na^+ , and, in correspondence with feature A4, it exhibits some residual current even after prolonged cycling. iii) Peak A3 exhibits essentially the same behavior as in the presence of Na^+ (Panel (A)). iv) Peak A4 is found at higher anodic potentials, in addition, it shifts to higher potentials than in the Na^+ -containing solution.

These changes witness the formation of different structures, a full characterization of which cannot be based solely on electrochemical and Raman measurements and will be the object of further studies. Nevertheless, some clear-cut conclusions can be drawn. On the one hand, the H^+ -intercalation process of features C0–C1 is less energetically favored, and, on the other hand, a more extensive reduction of the electrodeposit to Mn(II) takes

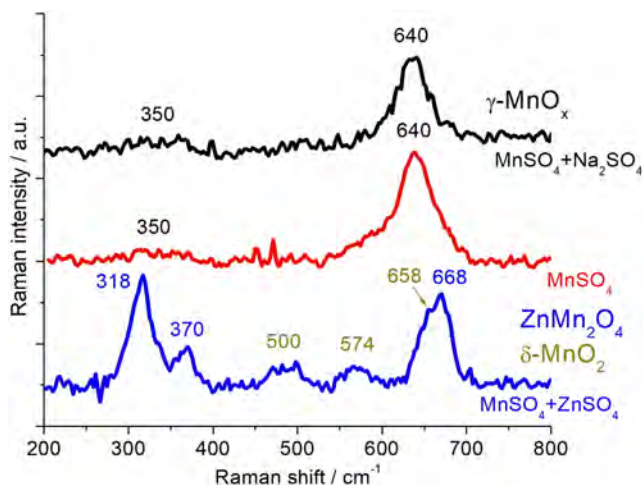


Figure 8. Raman spectra of electrodeposited EDM grown by CV from the following electrolytes: 4 mM MnSO_4 + 0.1 M Na_2SO_4 (black plot); 4 mM MnSO_4 (red plot) and 4 mM MnSO_4 + 0.1 M ZnSO_4 (blue plot).

place. In addition, full oxidation of the film requires higher potentials, owing to the progressive growth of poorly conducting material. Again, this phase formation process is compatible with the higher circulated anodic charge during cycling (Figure S2B, Supporting Information). The Raman spectrum of EDM grown from the 4 mM MnSO_4 solution (Figure 8, red plot) is the same as that we found for EDM electrodeposited from the electrolyte also containing 0.1 M Na_2SO_4 .

Adding Zn^{2+} to the Mn^{2+} -containing solution results in deep changes in the CVs (Figure 7C). The measurement reaches a very stable steady-state cycle, characterized by well-defined type-C1 and type-A2 peaks. Anodic charges are notably lower in the presence of Zn^{2+} ions, while cathodic charges remained unaltered, compared with Mn^{2+} -alone (Panel B) and Na^+ -containing solutions (Panel A). The c.d. does not exhibit a tendency to decrease upon cycling, and the consumed anodic and cathodic charges are very similar (Figure S2C, Supporting Information). This scenario is compatible with intercalation/deintercalation of Zn^{2+} , without the formation of inhibiting phases. This behavior is similar to that found in the first voltammetric cycle of $\alpha\text{-MnO}_2$ (see Section 3.2). The Raman spectrum of EDM grown from the solution containing 4 mM MnSO_4 and 0.1 M ZnSO_4 (Figure 8, blue plot) is different from that of EDM electrodeposited in the absence of Zn^{2+} . The bands at ≈ 318 , 370, and 668 cm^{-1} are compatible with tetragonal spinel ZnMn_2O_4 ^[62–67] and those at ≈ 500 , 574, and 658 cm^{-1} with $\delta\text{-MnO}_2$.^[68] Spectral assignment on the basis of the literature cannot be definitive, and a rigorous structural analysis is beyond the scope of this paper, but the profoundly modified pattern witnesses a strong effect of Zn^{2+} on the electrocrystallization of EDM.

3.3.2. Behavior of EDM in the Presence of Zn^{2+} , in the Potential Range Relevant to ZIB Operation

The electrochemical behavior of EDM, electrodeposited as described in Section 3.3.1 and 2.1.3, was tested in the potential

range that is typical of ZIB operation ($0.0\pm 0.8\text{ V}_{\text{Ag}/\text{AgCl}}$) in neutral solutions without and with added Zn^{2+} (Figure 9).

In the case of EDM grown by CV from the $\text{MnSO}_4/\text{Na}_2\text{SO}_4$ electrolyte, a featureless and stable pseudocapacitive cycle can be observed with a Na_2SO_4 electrolyte (Figure 9A.1). Instead, in the ZnSO_4 electrolyte, the voltammetric pattern is quite different (Figure 9A.2). In fact, the first cycle shows a couple of Zn^{2+} -intercalation peaks of C1/A2 types, the potentials of which correspond to the main peaks observed during electrodeposition from the $\text{MnSO}_4/\text{ZnSO}_4$ electrolyte (Section 3.1). Interestingly, this couple of peaks fades away in the first few cycles. This result points out the fact that even though this characteristic couple of peaks correlates with the presence of Zn^{2+} in the electrolyte, stable cycles of the type observed in Figure 7C cannot be obtained in a solution containing only Zn^{2+} . In fact, the interaction of the EDM film with solution Zn^{2+} leads to an irreversible transformation - possibly favored by the hydration radius of the divalent cation -, correlating with a drastic loss of the initial capacity.

The same type of behavior is observed with an EDM film grown from the MnSO_4 (Figure 9B) and $\text{MnSO}_4/\text{ZnSO}_4$ electrolytes (Figure 9C). This result shows that the differences in the films grown in the different electrolytes do not impact the interaction with Zn^{2+} . In fact, voltammetric cycling in the same electrolytes of EDM either electrodeposited with the combined galvanostatic/potentiostatic protocol of Section 2.1.3 (Figure 10A) or grown by CV, yields the same behavior: stable pseudocapacitive cycles in Na_2SO_4 and rapid fade of the C1/A2 peak pattern in ZnSO_4 .

3.3.3. Behavior of EDM in the Presence of Zn^{2+} and Mn^{2+} , in the Potential Range Relevant to ZIB Operation

In Section 3.2 and 3.3.2, we have observed that $\alpha\text{-MnO}_2$ and EDM, respectively, undergo a notable capacity fade in the Zn^{2+} -containing electrolyte. In the literature, Mn^{2+} is often added to Zn^{2+} -based neutral electrolytes with vague indications of the fact that this species favors cycling stability.^[69,70] The present subsection concentrates on the cycling behavior of EDM in electrolytes containing both Zn^{2+} and Mn^{2+} . Specifically, we concentrated on EDM electrodeposited onto carbon paper according to the procedure described in Section 2.1.3, cycled in the same $\text{MnSO}_4 + \text{ZnSO}_4$ electrolyte used for electrodeposition.

Replicated experiments were carried out in three- and two-electrode configurations and by varying the cycling conditions (for details, see the Supporting Information), yielding a coherent scenario. A representative selection of results is reported in Figure 10B.

The CV behavior is dominated by features A2 and C1, attributed to Zn^{2+} intercalation and deintercalation into and from EDM (see Section 3.1), as confirmed by the fact that the charges under the anodic and cathodic peaks match accurately. Prolonged cycling shows a slight, progressive capacity fade, related to transient structural rearrangements that deserve further study. The pristine capacity can be restored after a given cycling period, if the galvanostatic/potentiostatic protocol is repeated.

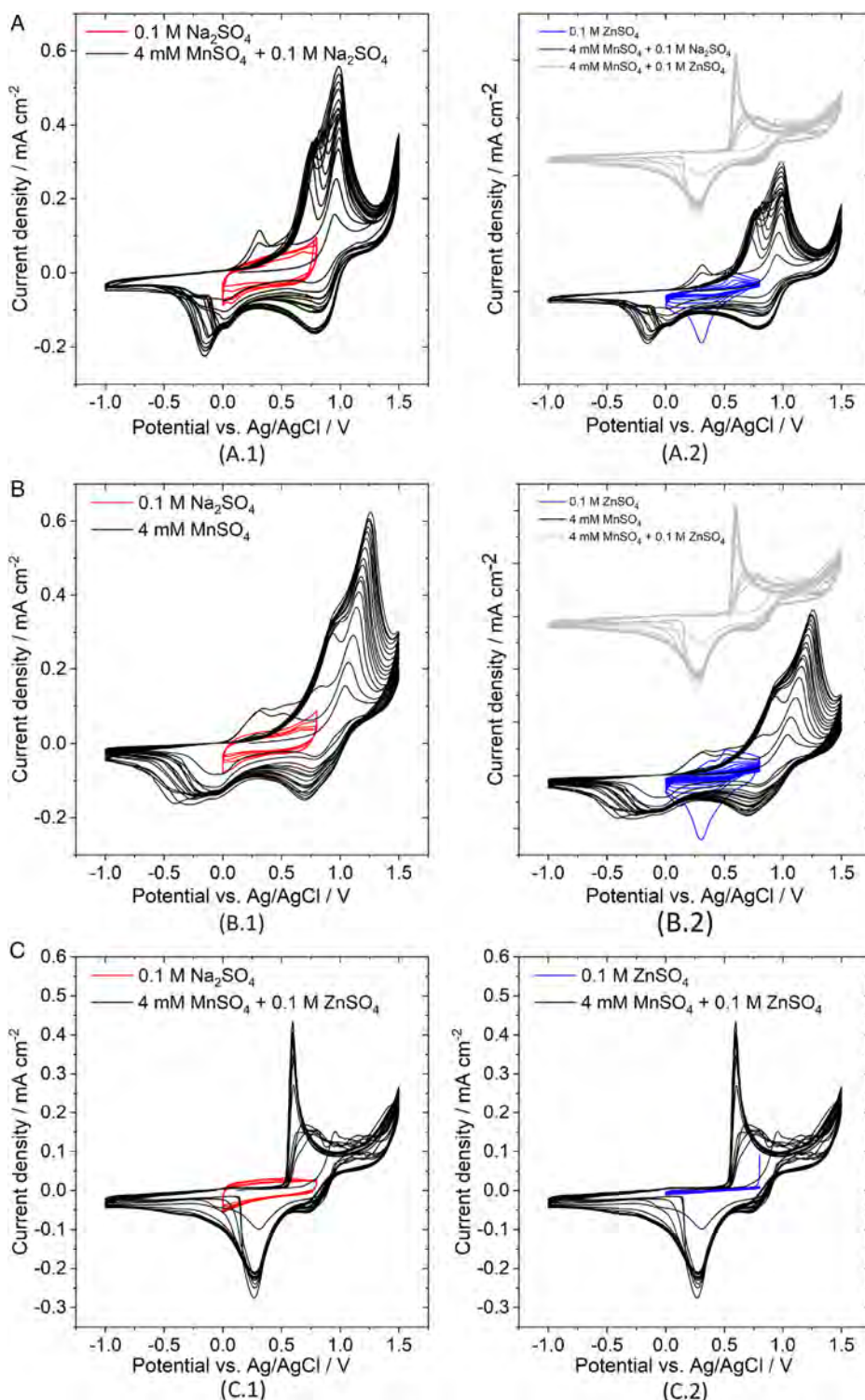


Figure 9. CVs of EDM films, electrodeposited from the following neutral electrolytes: A) 4 mM MnSO_4 + 0.1 M Na_2SO_4 , B) 4 mM MnSO_4 , and C) 4 mM MnSO_4 + 0.1 M ZnSO_4 . Red and blue plots denote CVs measured in the operating range of a ZIB cathode; black and gray plots correspond to CVs measured during the EDM electrodeposition process (see Figure 7). In particular, the gray plots in Panels (A2) and (B2) show the CV measured during electrodeposition from the 4 mM MnSO_4 + 0.1 M ZnSO_4 solution, for comparison. Test at potentials in the ZIB operating range was carried out in the following solutions: (A1, B1, C1) 0.1 M Na_2SO_4 ; (A2, B2, C2) 0.1 M ZnSO_4 . Glassy carbon support, scan rate 0.5 mV s^{-1} .

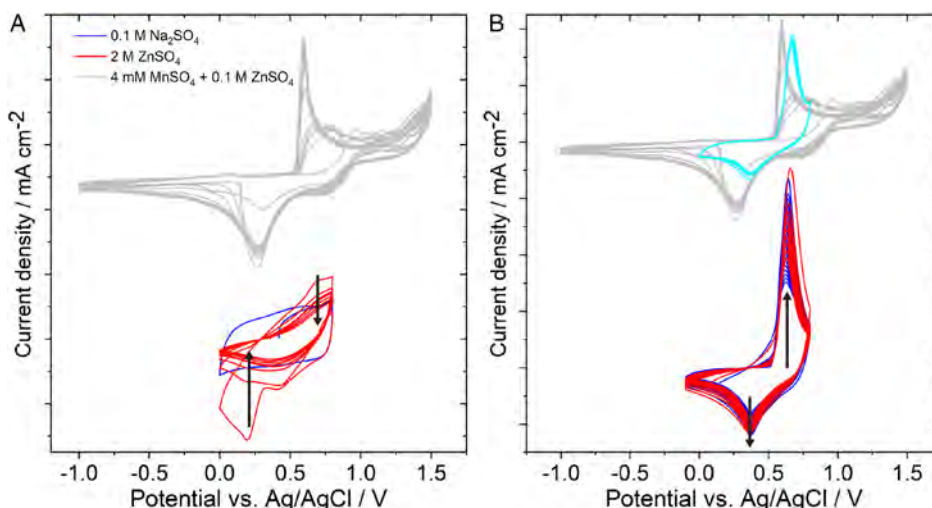


Figure 10. CVs measured in the operating range of a Zn-ion battery (ZIB) cathode for EDM film grown by galvanostatic/potentiostatic electrodeposition from a 0.2 M $\text{MnSO}_4 + 2 \text{ M ZnSO}_4$ neutral electrolyte. Carbon paper support, scan rate 0.5 mV s^{-1} . The upper, grey plots report the CV measured during electrodeposition from the 4 mM $\text{MnSO}_4 + 0.1 \text{ M ZnSO}_4$ solution, for comparison. A) Blue plot: 0.1 M Na_2SO_4 electrolyte, red plot: 2 M ZnSO_4 electrolyte. B) 0.2 M $\text{MnSO}_4 + 2 \text{ M ZnSO}_4$ neutral electrolyte. The blue and red plots of Panel (B) refer to sequential experiments, repeated with the same electrode, after having electrodeposited a fresh EDM film. The light-blue of Panel (B) compares a replicated measurement obtained in the same conditions, but in a split cell (see Supporting Information).

3.4. Impact of Zn^{2+} on the ORR Electrocatalytic Activity of $\alpha\text{-MnO}_2$: Case of ZAB Degradation

The ORR electrocatalytic activity of $\alpha\text{-MnO}_2$ in alkaline ambient was tested in the absence and in the presence of added Zn^{2+} in different electrolytes of practical interest for the present- and next-generation ZABs, with a combination of electrochemical approaches that yields a comprehensive comparative scenario. On the basis of the results of Section 3.2, Section S2, Supporting Information, and previous works in our group^[71,72] - that have highlighted the progressive ORR activation of as-fabricated MnO_2 -based electrocatalysts -, the electrodes were initially cycled to stabilize the chemical state of the compound. Then, electrode rotation-rate dependent measurements in RDE configuration were carried out, in order to derive information on the ORR mechanism prevailing in the different conditions. A consistency check was also performed with the RRDE configuration (Section S6, Supporting Information).

3.4.1. ORR Electrocatalysis in Alkaline Electrolytes

The results of experiments carried out in alkaline ambient without and with added Zn^{2+} are collected in **Figure 11**. Panel (A) confirms the literature behavior of MnO_2 in alkaline environment without Zn^{2+} ,^[73] which has also been the object of recent DFT-based investigation.^[74]

With the CVs in Ar-saturated electrolyte, in the first cycle, it is possible to note a prominent cathodic main peak centered at $-0.4 \text{ V}_{\text{SHE}}$, associated with the reduction from Mn^{4+} to poorly reversible mixed oxi-hydroxide $\text{MnOOH}/\text{Mn}(\text{OH})_2$ (see Section 3.1, Section S1.4, and S2, Supporting Information). The stable cathodic features centered around $\approx -0.15 \text{ V}_{\text{SHE}}$ can be associated with proton intercalation into MnO_2 . The

anodic peak centered at $\approx 0.15 \text{ V}_{\text{SHE}}$ corresponds to proton deintercalation from HMnO_2 . In the O_2 -saturated solution without Zn^{2+} , the ORR limiting c.d. reaches a value of $\approx -5 \text{ mA cm}^{-2}$, which slightly decreases.

In the de-aerated solution (Panels (A) and (C)), the addition of Zn^{2+} brings forward both the cathodic and anodic peaks in the first CV cycle to ≈ -0.37 and 0 V_{SHE} , coherently with our findings of Section 3.2. With O_2 saturation, the limiting c.d. is found to be a factor of 2 lower. The rotation-rate-dependent LSVs, reported in Figure 11B,D, have been elaborated with the Koutecký–Levich method (see Section S6, Supporting Information for some details), the results of which are summarized in Figure 11E). Within the limits of the experimental accuracy of Koutecký–Levich modeling of electrocatalysts with a multiplicity of active sites, our data hint at an apparent four-electron oxygen reduction mechanism,^[53–56,73] for both the electrolytes without and with added Zn^{2+} . The Koutecký–Levich approach is very useful to classify ORR electrocatalyst mechanisms into the two- and four-electron types, but it exhibits some limits in the exact determination of electron transfer number n , in fact, this method assumes a single-step reaction, whereby n would depend on the RDE angular velocity.^[75] Therefore, even though the presence of Zn^{2+} in solution does not influence the ORR reaction mechanism as such – as synthetically represented by the comparison of the LSV curves at 1600 rpm shown in Figure 11F –, it is possible to note both the higher onset potential and the lower limiting c.d. for the Zn^{2+} -containing system, suggesting a lower performance of the catalyst in this environment. SEM micrographs of the electrode after RDE ORR tests in the presence of Zn^{2+} show that the homogeneous fibrous surface morphology of the pristine electrode (**Figure 12A**) changes to a heterogeneous one (**Figure 12B**), partially covered with a water-insoluble Zn-containing film (**Figure 12F**).

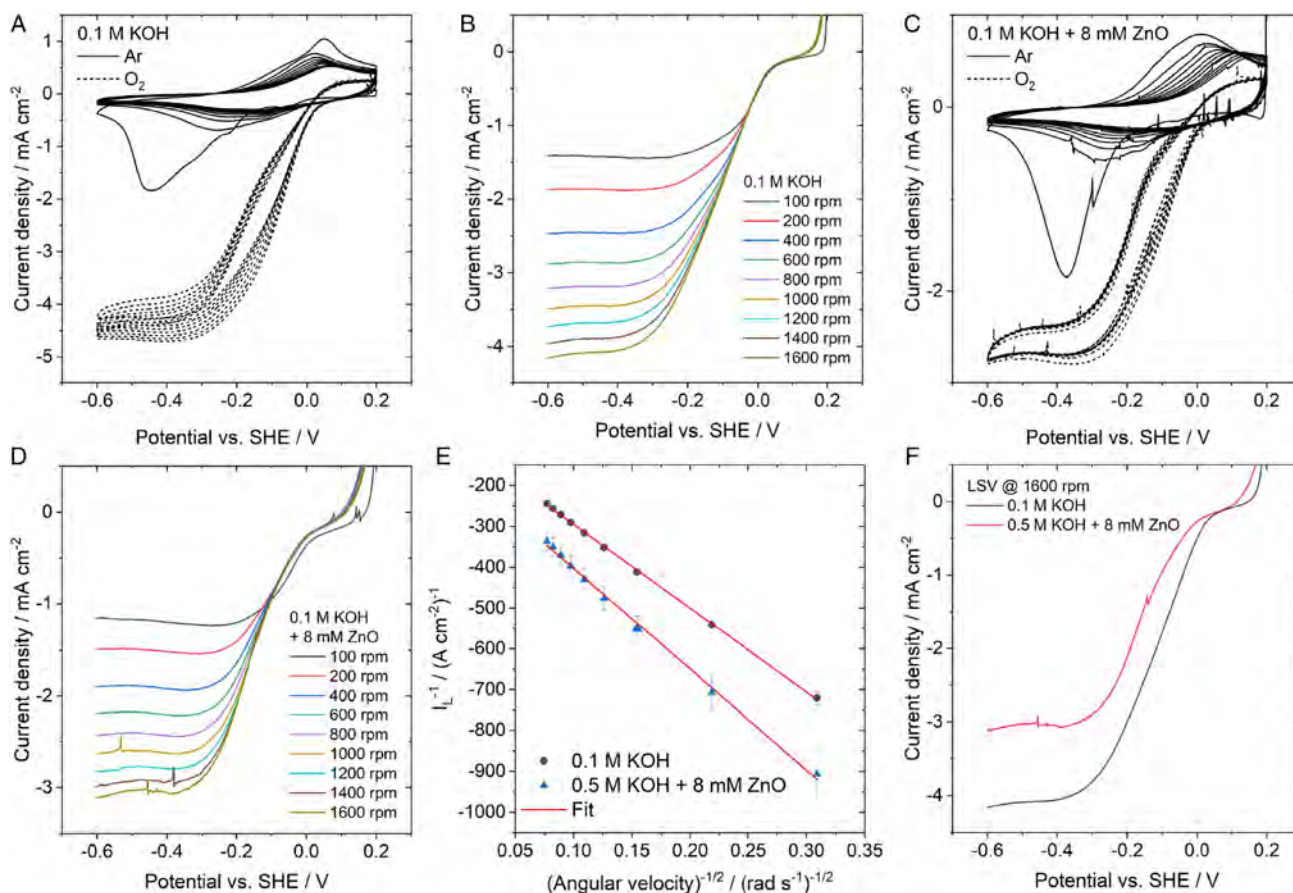


Figure 11. Rotating disk electrode (RDE) oxygen reduction reaction (ORR) experiments with α -MnO₂ electrodes in alkaline electrolyte A,B) without and C,D) with added Zn²⁺. A,C) CV measurements in Ar-saturated (solid line) and O₂-saturated (dashed line) electrolytes, at 1600 rpm; B,D) linear-sweep voltammetry (LSV) measurements as a function of rotation rate; E) Koutecky–Levich plots estimated without and with added Zn²⁺: the current density at -0.5 V_{SHE} was assimilated to i_L . The error bars were estimated from sets of three independent replicated experiments. F) Comparison between LSVs measured in absence and presence of Zn²⁺ at 1600 rpm.

The Raman spectrum of the electrode after the RDE ORR measurements in the presence of Zn²⁺ is shown in **Figure 13** (red plot) and compared with the spectrum of the pristine electrode (black plot). The spectrum of the pristine material is commented on in Section 3.2.: here we have extended the Raman shift range to encompass also other bands of the transformed material and the graphite D and G bands at 1317 and 1597 cm⁻¹, respectively, are also shown. It can be noticed that a profound change in spectra pattern is found, corresponding to the formation of a new phase that can be assigned to the tetragonal spinel ZnMn₂O₄ (see Section 3.3.1 above).

3.4.2. ORR Electrocatalysis in Neutral Electrolytes

Neutral electrolytes are raising research interest for rechargeable ZABs,^[76] owing to better cycling performance of the Zn anode,^[16] but ORR electrocatalysis of manganese oxides in this ambient has not been investigated in depth, so far. Moreover, no information is available on the impact of Zn²⁺ on ORR performance.

In **Figure 14**, we report RDE ORR measurements with the neutral sulfate electrolyte without and with added Zn²⁺.

Complementary tests have been carried out in a Leclanché-type neutral electrolyte, which are reported in Section S7, Supporting Information. In the sulfate solution without added Zn²⁺ (Figure 14A,B), the ORR onset potential is retarded with respect to the alkaline electrolyte, but, as expected, the c.d. reaches values around 4 mA cm⁻², which are close to those found in alkaline at the same rotation rate. With this electrolyte, no well-defined limiting c.d. is reached: this behavior is common in the literature on ORR electrocatalysts by manganese oxide-based materials, and has been attributed to the presence of a multiplicity of catalytic sites.^[77–79] The fact that the same material yields a well-defined limiting current in alkaline electrolyte, but not in the neutral sulfate one, is a clear indication of the difference in ORR mechanism in the two ambients. The number of transferred electrons n was estimated – within experimental and fitting errors – to be ≈ 4 , in accord with.^[77]

The presence of Zn²⁺ in the solution causes a strong effect on both the CV and the LSV curves, leading to a rapid decrease of the c.d. (Figure 14D–F). In particular, the shapes of the CV curves bear a similarity with those investigated in Section 3.2, denoting irreversible phase formation in the presence of Zn²⁺ in the electrolyte. The lack of a measurable dependence of the LSVs on the

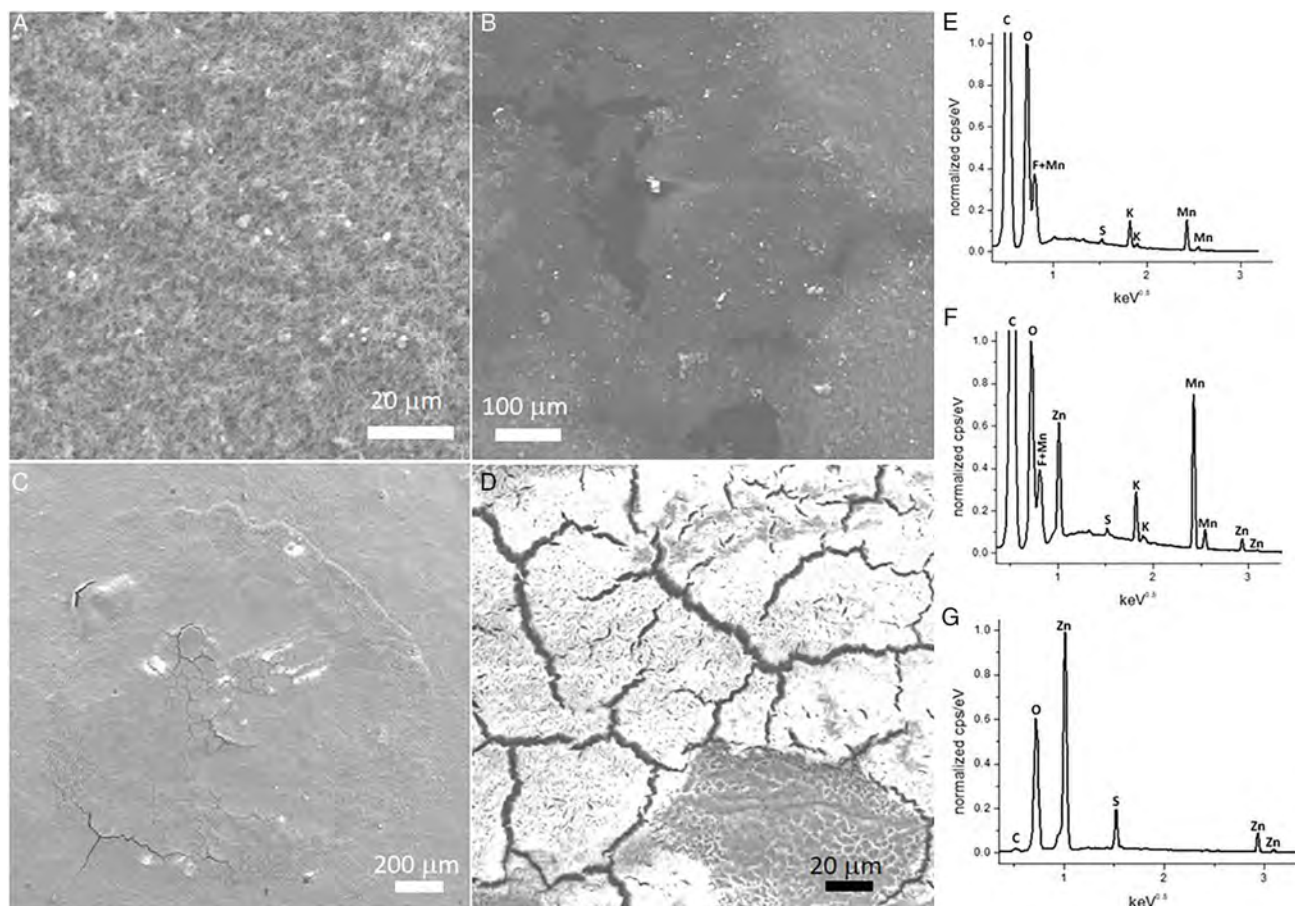


Figure 12. A–D) SEM micrographs) and E–G) EDS spectra of α - MnO_2 electrodes. A,E) pristine conditions; B,F) after RDE ORR test in an alkaline solution containing Zn^{2+} (see Figure 11); C,D,G) after RDE ORR test in neutral sulfate solution containing Zn^{2+} (see Figure 14).

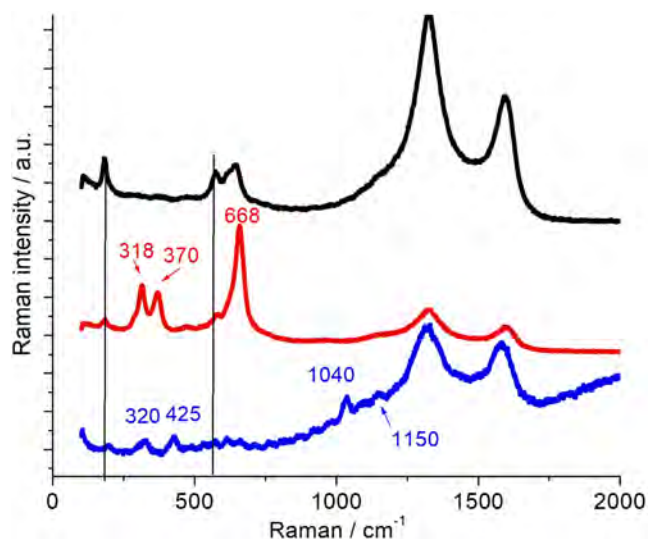


Figure 13. Raman spectra of α - MnO_2 electrodes in pristine conditions (black plot), after RDE ORR test in an alkaline solution containing Zn^{2+} (red plot) and after RDE ORR test in neutral sulfate solution containing Zn^{2+} (blue plot).

rotation rate (Figure 14E) prevents an estimate of the number of exchanged electrons.

The SEM images of the electrode after ORR testing in the sulfate-based neutral electrolyte containing Zn^{2+} (Figure 12C,D) highlight the formation of a water-insoluble thick, cracked layer of Zn-containing (Figure 12G) material, that is responsible for the passivation of the electrocatalyst.

The Raman spectrum of the electrode after the RDE ORR measurements in the presence of Zn^{2+} is shown in Figure 13 (blue plot) and compared with the spectrum of the pristine electrode (black plot). Also, in this case, the modified spectral pattern can be attributed, on the basis of the literature, to Gunningite $\text{Zn}(\text{H}_2\text{O})_5\text{OSO}_3$. Ref. [80] discusses thoroughly the sulfate-related bands of this compound and assigns the bands at 1040 and 1150 cm^{-1} to ν_3 combination modes of SO_4^{2-} in the characteristic bidentate complex configuration and the band at 425 cm^{-1} to the ν_2 mode of SO_4^{2-} . The same paper does not interpret the modes at 320 cm^{-1} , which can be assigned to either $\nu(\text{Zn-O})$ ^[81] or $\nu(\text{Zn-S})$ ^[82]. It is worth noting that another, but different type of sulfate-containing Zn(II)-based basic salt has been reported to form as a result of the cycling of Zn electrodes in neutral sulfate-containing electrolytes: zinc hydroxyl-sulfate $\text{Zn}_4(\text{OH})_6\text{SO}_4 \cdot \text{aq}$.^[83,84]

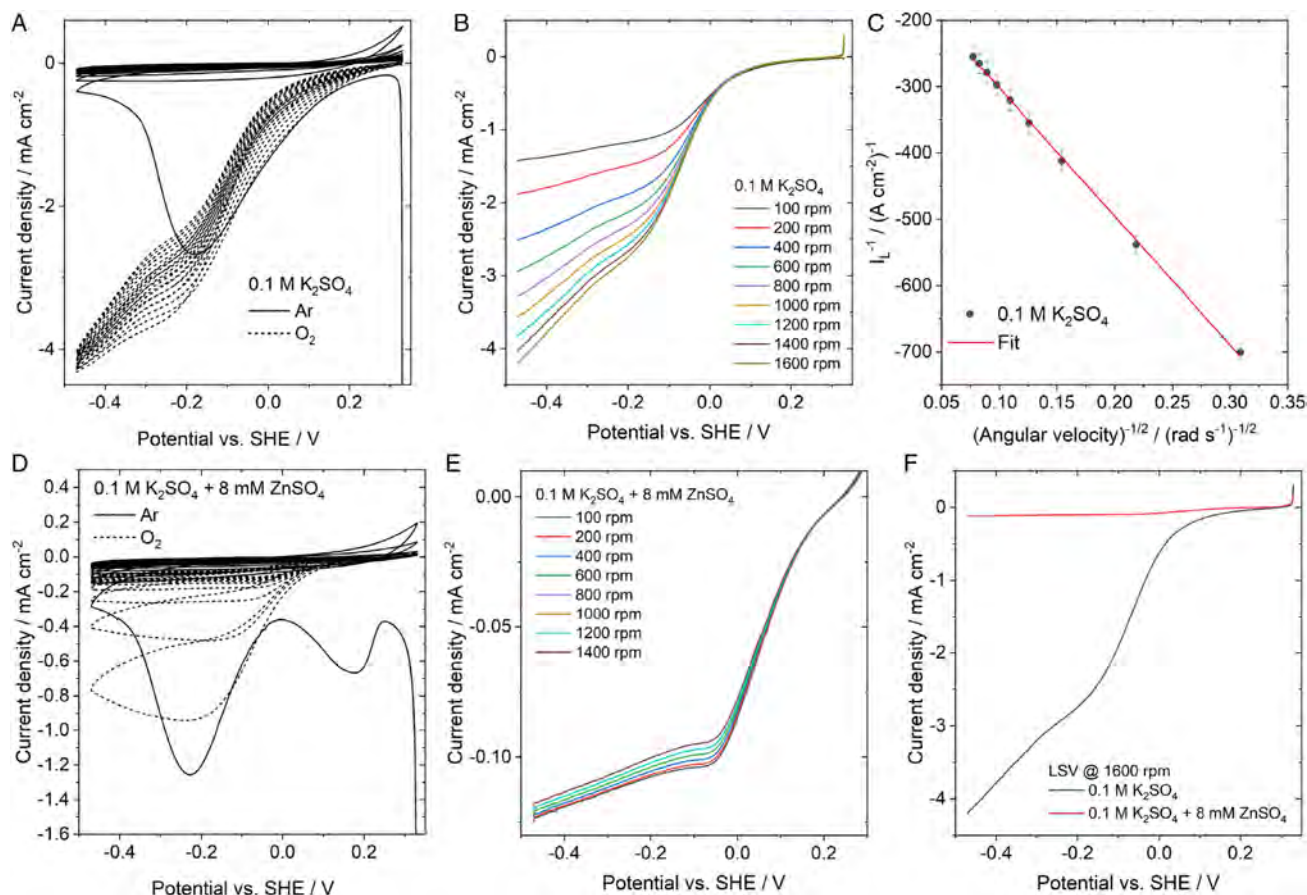


Figure 14. RDE ORR experiments with α -MnO₂ electrodes in neutral sulfate electrolyte A,B) without and D) with added Zn²⁺. A,D) CV measurements in Ar-saturated (solid line) and O₂-saturated (dashed line) electrolytes, at 1600 rpm; B,E) LSV measurements as a function of rotation rate; C) Koutecky–Levich plots estimated without added Zn²⁺: the current density at -0.2 V vs V_{SHE} was assimilated to i_L . The error bars were estimated from sets of three independent replicated experiments. F) Comparison between LSVs measured in absence and presence of Zn²⁺ at 1600 rpm.

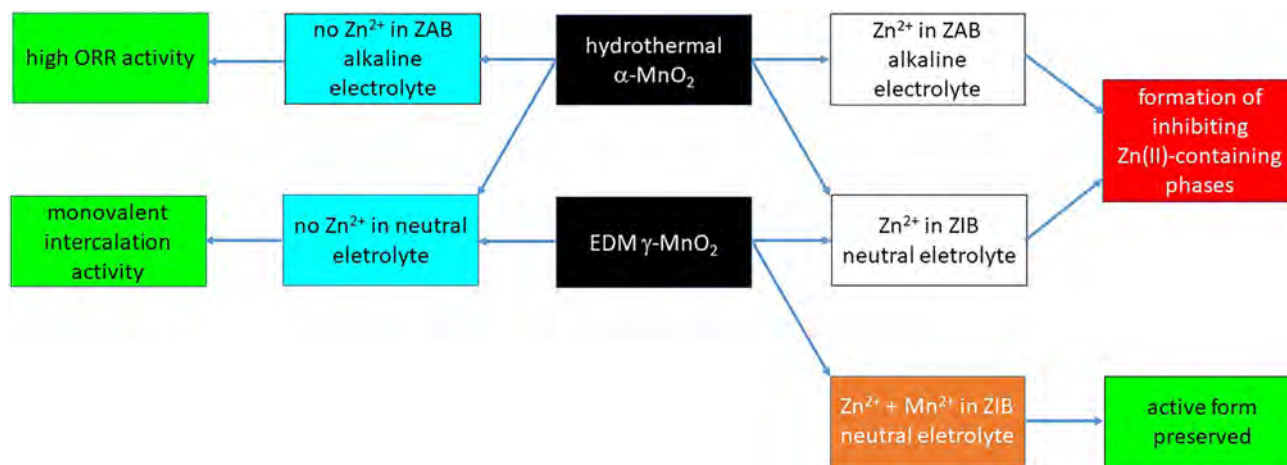


Figure 15. Schematic of the fate of the electrochemical performance of hydrothermal α -MnO₂ and γ -MnO₂ EDM in zinc–air battery (ZAB)- and ZIB- type electrolytes, in the absence and the presence of Zn²⁺.

4. Conclusions

Systematic comparative electrochemical investigation of α -MnO₂ and γ -MnO₂ type EDM in neutral and alkaline ambients, relevant to ZIB and ZAB technologies, has evidenced that added Zn²⁺ gives rise to irreversible material transformations, that tend to deactivate cathodic functionality.

Specifically, under ZIB operating conditions (neutral ambient), hydrothermally grown α -MnO₂ initially behaves in a way that can be interpreted in terms of intercalation, but soon it deactivates irreversibly. Potentiostatic polarization in conditions representative of ZIB deep discharge, without and with subsequent charge, shows evident phase transformations, correlating with a modification of the morphology of the cryptomelane nanorods.

The excellent ORR activity of α -MnO₂ is rapidly degraded when Zn²⁺ is added to the alkaline electrolyte. This degradation does not seem to impact the ORR mechanism, but the onset potential and the reduction c.d. are affected by what seems to be the formation of a layer of spinel ZnMn₂O₄. Even more dramatic degradation of ORR activity is found in neutral sulfate ambient, where a thick layer of Zn₄(OH)₆SO₄ passivates the electrode.

EDM grown by voltammetric cycling from neutral MnSO₄ solutions shows a deeply different electrochemical response in the absence and in the presence of Zn²⁺. The voltammetric pattern found in the Mn²⁺/Zn²⁺ solution is compatible with Zn²⁺ intercalation, and Raman spectroscopy reveals that the α -MnO₂ structure found without Zn²⁺, changes to tetragonal spinel ZnMn₂O₄ when Zn²⁺ is added. Operation of EDM in the ZIB potential range in neutral solution clearly shows that the pseudocapacitive behavior found in the absence of Zn²⁺ - can be explained with intercalation of H⁺ or Na⁺ -, is lost when Zn²⁺ is added: no electrochemical activity is found in either discharge or charge conditions.

The electrochemical response is instead totally changed if Mn²⁺ is added together with Zn²⁺: cathodic discharge activity is restored, and the electrode responds anodically when charging conditions are applied, in essence, because electrodeposition conditions are enabled by solution-phase Mn²⁺.

The global message of this work is thus that Zn²⁺, as such, interacts with α -MnO₂ and EDM in aqueous ambients of different pH in different ways, depending on the crystallographic type and on the pH, in all cases leading to irreversible degradation of cathode performance. Degradation can be due to the formation of mixed Zn/Mn oxides - as in alkaline ORR conditions for α -MnO₂ and in neutral ZIB conditions for EDM -, or to the formation of a Zn²⁺ basic salt passivating layer for α -MnO₂-as in neutral ORR conditions. ZIB operation can be stabilized if spinel ZnMn₂O₄ electrodeposition conditions are tacitly established, but - in view of real-world implementation of ZIB technology - this would require a more insightful evaluation of the impact on practical electrode capacity. These conclusions are schematized in **Figure 15**.

In conclusion, we can state that, on the one hand, the topic of Zn²⁺ interaction with MnO₂ deserves more extensive investigation for different allotropes, in different ambients and with different analysis methods, and, on the other hand, in ZAB processes access of Zn²⁺ to the MnO₂-based electrocatalyst should be avoided, either by appropriate complexing

(see Section S7, Supporting Information for preliminary results) or by use of ion-selective membranes.

Supporting Information

Supporting Information is available from the Wiley Online Library or from the author.

Acknowledgements

Some of the CV data reported in this work were collected in the framework of Abdurrahmane Safa Okšaš's MSc thesis at the Department of Energy of Politecnico di Milano: his support for experimental activity is gratefully acknowledged.

Open Access Funding provided by Politecnico di Milano within the CRUI-CARE Agreement.

Conflict of Interest

The authors declare no conflict of interest.

Data Availability Statement

The data that support the findings of this study are available from the corresponding author upon reasonable request.

Keywords

cryptomelane, manganese dioxide, ORR, zinc-air batteries, zinc-ion batteries

Received: January 23, 2022

Revised: May 22, 2022

Published online: July 1, 2022

- [1] F. Duffner, N. Kronemeyer, J. Tübke, J. Leker, M. Winter, R. Schmich, *Nat. Energy* **2021**, *6*, 123.
- [2] H. Li, W. Zhang, K. Sun, J. Guo, K. Yuan, J. Fu, T. Zhang, X. Zhang, H. Long, Z. Zhang, Y. Lai, H. Sun, *Adv. Energy Mater.* **2021**, *11*, 2100867.
- [3] Y. Shi, Y. Chen, L. Shi, K. Wang, B. Wang, L. Li, Y. Ma, Y. Li, Z. Sun, W. Ali, S. Ding, *Small* **2020**, *16*, 2000730.
- [4] F. Santos, A. Urbina, J. Abad, R. López, C. Toledo, A. J. Fernández Romero, *Chemosphere* **2020**, *250*, 126273.
- [5] T. Nagy, L. Nagy, Z. Erdélyi, E. Baradács, G. Deák, M. Zsuga, S. Kéki, *Electrochim. Acta* **2021**, *368*, 137592.
- [6] J. Zhang, Q. Zhou, Y. Tang, L. Zhang, Y. Li, *Chem. Sci.* **2019**, *10*, 8924.
- [7] J. Fu, Z. P. Cano, M. G. Park, A. Yu, M. Fowler, Z. Chen, *Adv. Mater.* **2017**, *29*, 1604685.
- [8] J. Fu, R. Liang, G. Liu, A. Yu, Z. Bai, L. Yang, Z. Chen, *Adv. Mater.* **2019**, *31*, 1805230.
- [9] D. Selvakumaran, A. Pan, S. Liang, G. Cao, *J. Mater. Chem. A* **2019**, *7*, 18209.
- [10] M. Song, H. Tan, D. Chao, H. J. Fan, *Adv. Funct. Mater.* **2018**, *28*, 1802564.
- [11] W. Shang, W. Yu, Y. Liu, R. Li, Y. Dai, C. Cheng, P. Tan, M. Ni, *Energy Storage Mater.* **2020**, *31*, 44.
- [12] *Periodic Reporting for period 1 - TT-Battery (Low cost, long durability rechargeable Green Battery based on Zn and MnO₂ electrodes.)* |

- H2020 | CORDIS | European Commission, <https://cordis.europa.eu/project/id/806940/reporting>, 2020.
- [13] C. Helbig, A. M. Bradshaw, L. Wietschel, A. Thorenz, A. Tuma, *J. Cleaner Production* **2018**, 172, 274.
- [14] S. Bobba, S. Carrara, J. Huisman, F. Mathieux, C. Pavel, *Critical Raw Materials for Strategic Technologies and Sectors in the EU - A Foresight Study*, <https://ec.europa.eu/docsroom/documents/42881>, 2020.
- [15] V. Mathew, B. Sambandam, S. Kim, S. Kim, S. Park, S. Lee, M. H. Alfaruqi, V. Soundharajan, S. Islam, D. Y. Putro, J.-Y. Hwang, Y.-K. Sun, J. Kim, *ACS Energy Lett.* **2020**, 5, 2376.
- [16] M. Kazemian, F. Rossi, A. Casaroli, T. Caielli, B. Kaulich, M. Kiskinova, B. Bozzini, *J. Power Sources* **2022**, unpublished.
- [17] F. Rossi, C. Mele, M. Boniardi, B. Bozzini, *ChemElectroChem* **2020**, 7, 1752.
- [18] F. Rossi, L. Mancini, I. Sgura, M. Boniardi, A. Casaroli, A. P. Kao, B. Bozzini, *ChemElectroChem* **2022**, 9, e202101537.
- [19] J. Ming, J. Guo, C. Xia, W. Wang, H. N. Alshareef, *Mater. Sci. Eng. R: Rep.* **2019**, 135, 58.
- [20] T. Wang, C. Li, X. Xie, B. Lu, Z. He, S. Liang, J. Zhou, *ACS Nano* **2020**, 14, 16321.
- [21] J. Shin, J. Lee, Y. Park, J. W. Choi, *Chem. Sci.* **2020**, 11, 2028.
- [22] Y. Zhang, Z. Chen, H. Qiu, W. Yang, Z. Zhao, J. Zhao, G. Cui, *NPG Asia Mater* **2020**, 12, 4.
- [23] C. Xu, B. Li, H. Du, F. Kang, *Angew. Chem.* **2012**, 124, 957.
- [24] K. Sada, B. Senthilkumar, P. Barpanda, *J. Mater. Chem. A* **2019**, 7, 23981.
- [25] M. H. Alfaruqi, J. Gim, S. Kim, J. Song, J. Jo, S. Kim, V. Mathew, J. Kim, *J. Power Sources* **2015**, 288, 320.
- [26] S. Islam, M. H. Alfaruqi, J. Song, S. Kim, D. T. Pham, J. Jo, S. Kim, V. Mathew, J. P. Baboo, Z. Xiu, J. Kim, *J. Energy Chem.* **2017**, 26, 815.
- [27] E. Marini, L. Jörisen, S. Brimaud, *J. Power Sources* **2021**, 482, 228900.
- [28] M. H. Alfaruqi, V. Mathew, J. Gim, S. Kim, J. Song, J. P. Baboo, S. H. Choi, J. Kim, *Chem. Mater.* **2015**, 27, 3609.
- [29] M. Chamoun, W. R. Brant, C.-W. Tai, G. Karlsson, D. Noréus, *Energy Storage Mater.* **2018**, 15, 351.
- [30] C. J. Clarke, G. J. Browning, S. W. Donne, *Electrochim. Acta* **2006**, 51, 5773.
- [31] P. Ruetschi, *J. Electrochem. Soc.* **1988**, 135, 7.
- [32] P. Ruetschi, *J. Electrochem. Soc.* **1984**, 8, 2737.
- [33] J. W. Gallaway, M. Menard, B. Hertzberg, Z. Zhong, M. Croft, L. A. Sviridov, D. E. Turney, S. Banerjee, D. A. Steingart, C. K. Erdonmez, *J. Electrochem. Soc.* **2015**, 162, A162.
- [34] R. Patrice, B. Gerand, J. B. Leriche, L. Seguin, E. Wang, R. Moses, K. Brandt, J. M. Tarascon, *J. Electrochem. Society* **2001**, 148, A448.
- [35] C. Mondoloni, M. Laborde, J. Rioux, C. Levy-Clement, *J. Electrochem. Soc.* **1992**, 139, 954.
- [36] J. Shin, J.-M. You, J. Z. Lee, R. Kumar, L. Yin, J. Wang, Y. Shirley Meng, *Phys. Chem. Chem. Phys.* **2016**, 18, 26376.
- [37] W. Sun, F. Wang, S. Hou, C. Yang, X. Fan, Z. Ma, T. Gao, F. Han, R. Hu, M. Zhu, C. Wang, *J. Am. Chem. Soc.* **2017**, 139, 9775.
- [38] S.-D. Han, S. Kim, D. Li, V. Petkov, H. D. Yoo, P. J. Phillips, H. Wang, J. J. Kim, K. L. More, B. Key, R. F. Klie, J. Cabana, V. R. Stamenkovic, T. T. Fister, N. M. Markovic, A. K. Burrell, S. Tepavcevic, J. T. Vaughey, *Chem. Mater.* **2017**, 29, 4874.
- [39] H. Pan, Y. Shao, P. Yan, Y. Cheng, K. S. Han, Z. Nie, C. Wang, J. Yang, X. Li, P. Bhattacharya, K. T. Mueller, J. Liu, *Nat Energy* **2016**, 1, 16039.
- [40] B. Lee, C. S. Yoon, H. R. Lee, K. Y. Chung, B. W. Cho, S. H. Oh, *Sci. Rep.* **2015**, 4, 6066.
- [41] X. Guo, J. Zhou, C. Bai, X. Li, G. Fang, S. Liang, *Mater. Today Energy* **2020**, 16, 100396.
- [42] C. Wang, J. Li, Z. Zhou, Y. Pan, Z. Yu, Z. Pei, S. Zhao, L. Wei, Y. Chen, *EnergyChem* **2021**, 3, 100055.
- [43] A. R. Mainar, E. Iruin, L. C. Colmenares, A. Kvasa, I. de Meatza, M. Bengoechea, O. Leonet, I. Boyano, Z. Zhang, J. A. Blazquez, *J. Energy Storage* **2018**, 15, 304.
- [44] G. Fang, J. Zhou, A. Pan, S. Liang, *ACS Energy Lett.* **2018**, 3, 2480.
- [45] T. N. T. Tran, S. Jin, M. Cuisinier, B. D. Adams, D. G. Ivey, *Sci. Rep.* **2021**, 11, 20777.
- [46] L. Wang, J. Wang, F. Jia, C. Wang, M. Chen, *J. Mater. Chem. A* **2013**, 1, 9498.
- [47] E. D. Rus, G. D. Moon, J. Bai, D. A. Steingart, C. K. Erdonmez, *J. Electrochem. Soc.* **2016**, 163, A356.
- [48] J. Shin, J. K. Seo, R. Yaylian, A. Huang, Y. S. Meng, *Int. Mater. Rev.* **2020**, 65, 356.
- [49] C. Julien, A. Mauger, *Nanomaterials* **2017**, 7, 396.
- [50] N. Larabi-Gruet, S. Peulon, A. Lacroix, A. Chaussé, *Electrochim. Acta* **2008**, 53, 7281.
- [51] L. E. Blanc, D. Kundu, L. F. Nazar, *Joule* **2020**, 4, 771.
- [52] F. Wan, L. Zhang, X. Dai, X. Wang, Z. Niu, J. Chen, *Nat Commun* **2018**, 9, 1656.
- [53] T. Gao, H. Fjellvåg, P. Norby, *Anal. Chim. Acta* **2009**, 648, 235.
- [54] T. Gao, M. Glerup, F. Krumeich, R. Nesper, H. Fjellvåg, P. Norby, *J. Phys. Chem. C* **2008**, 112, 13134.
- [55] M. Polverejan, J. C. Villegas, S. L. Suib, *J. Am. Chem. Soc.* **2004**, 126, 7774.
- [56] M. Wei, Y. Konishi, H. Zhou, H. Sugihara, H. Arakawa, *Nanotechnology* **2005**, 16, 245.
- [57] C. M. Julien, M. Massot, C. Poinignon, *Spectrochim. Acta, Part A* **2004**, 60, 689.
- [58] C. Julien, M. Massot, S. Rangan, M. Lemal, D. Guyomard, *J. Raman Spectrosc.* **2002**, 33, 223.
- [59] M. Xiong, M. P. Clark, M. Labbe, D. G. Ivey, *J. Power Sources* **2018**, 393, 108.
- [60] E. Marini, D. Oliveira De Souza, G. Aquilanti, M. Liebert, F. Rossi, B. Bozzini, *Appl. Sci.* **2021**, 11, 11672.
- [61] M. Ndjeri, S. Peulon, S. Bach, A. Chaussé, *Electrochim. Acta* **2011**, 56, 8564.
- [62] H. Li, B. Song, W. J. Wang, X. L. Chen, *Mater. Chem. Phys.* **2011**, 130, 39.
- [63] K. Samanta, S. Dussan, R. S. Katiyar, P. Bhattacharya, *Appl. Phys. Lett.* **2007**, 90, 261903.
- [64] Q. Sun, M. Bijelić, A. B. Djuričić, C. Suchomski, X. Liu, M. Xie, A. M. C. Ng, H. Kong Li, K. Shih, S. Burazer, Ž. Skoko, I. Djerdj, J. Popović, *Nanotechnology* **2017**, 28, 455401.
- [65] C. Shamitha, T. Senthil, L. Wu, B. S. Kumar, S. Anandhan, *J. Mater. Sci.: Mater. Electron.* **2017**, 28, 15846.
- [66] L. Malavasi, P. Galinetto, M. C. Mozzati, C. B. Azzoni, G. Flor, *Phys. Chem. Chem. Phys.* **2002**, 4, 3876.
- [67] M. Tortosa, F. J. Manjón, M. Mollar, B. Marí, *J. Phys. Chem. Solids* **2012**, 73, 1111.
- [68] Y. Xie, Y. Yu, X. Gong, Y. Guo, Y. Guo, Y. Wang, G. Lu, *CrystEngComm* **2015**, 17, 3005.
- [69] V. Soundharajan, B. Sambandam, S. Kim, S. Islam, J. Jo, S. Kim, V. Mathew, Y. Sun, J. Kim, *Energy Storage Mater.* **2020**, 28, 407.
- [70] Y. Huang, J. Mou, W. Liu, X. Wang, L. Dong, F. Kang, C. Xu, *Nano-Micro Lett.* **2019**, 11, 49.
- [71] P. Bocchetta, B. Alemán, M. Amati, M. Fanetti, A. Goldoni, L. Gregoratti, M. Kiskinova, C. Mele, H. Sezen, B. Bozzini, *Electrochem. Commun.* **2016**, 69, 50.
- [72] B. Bozzini, P. Bocchetta, A. Gianoncelli, C. Mele, M. Kiskinova, *ChemElectroChem* **2015**, 2, 1541.
- [73] F. Cheng, Y. Su, J. Liang, Z. Tao, J. Chen, *Chem. Mater.* **2010**, 22, 898.
- [74] M. Rittirum, S. Somdee, P. Buapin, N. Aumngongpho, N. Kerdpravit, T. Saelee, S. Kheawhom, N. Chotigkrai, S. Praserttham, P. Praserttham, *J. Alloys Compd.* **2021**, 869, 159280.

- [75] R. Zhou, Y. Zheng, M. Jaroniec, S.-Z. Qiao, *ACS Catal.* **2016**, *6*, 4720.
- [76] S. Clark, A. Latz, B. Horstmann, *ChemSusChem* **2017**, *10*, 4735.
- [77] I. Roche, K. Scott, *J. Electroanal. Chem.* **2010**, *638*, 280.
- [78] P. Bocchetta, A. Gianoncelli, M. K. Abyaneh, M. Kiskinova, M. Amati, L. Gregoratti, D. Jezeršek, C. Mele, B. Bozzini, *Electrochim. Acta* **2014**, *137*, 535.
- [79] B. Bozzini, P. Bocchetta, G. Kourousias, A. Gianoncelli, *Polymers* **2017**, *9*, 17.
- [80] W. W. Rudolph, M. H. Brooker, P. R. Tremaine, *J. Solution Chem.* **1999**, *28*, 621.
- [81] M. Wang, L. Jiang, E. J. Kim, S. H. Hahn, *RSC Adv.* **2015**, *5*, 87496.
- [82] A. Torreggiani, A. Tinti, *Metallomics* **2010**, *2*, 246.
- [83] T. Xin, Y. Wang, N. Wang, Y. Zhao, H. Li, Z. Zhang, J. Liu, *J. Mater. Chem. A* **2019**, *7*, 23076.
- [84] W. Xin, L. Miao, L. Zhang, H. Peng, Z. Yan, Z. Zhu, *ACS Mater. Lett.* **2021**, *3*, 1819.